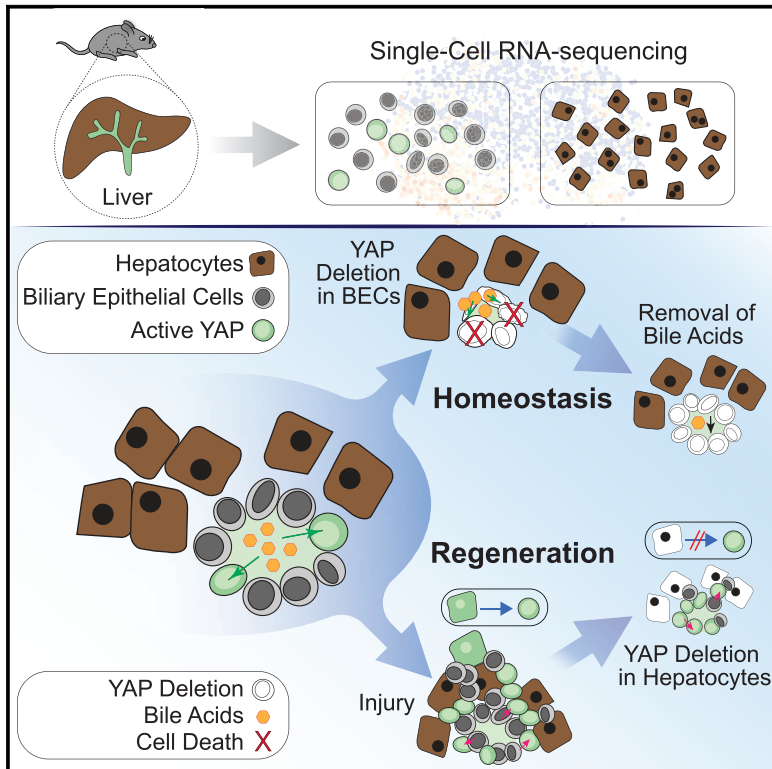


Cell Stem Cell

Single-Cell Analysis of the Liver Epithelium Reveals Dynamic Heterogeneity and an Essential Role for YAP in Homeostasis and Regeneration

Graphical Abstract



Authors

Brian J. Pepe-Mooney, Michael T. Dill, Anna Alemany, ..., Alex K. Shalek, Alexander van Oudenaarden, Fernando D. Camargo

Correspondence

fernando.camargo@childrens.harvard.edu

In Brief

The transcriptional landscape of the epithelium in healthy and regenerating murine livers was investigated, revealing a dynamically fluctuating and heterogeneous YAP transcriptional program. Further analysis uncovered YAP signaling dualism: it is essential in biliary epithelial cells for homeostatic maintenance and in hepatocytes for the regenerative response to injury.

Highlights

- scRNA-seq of the healthy and injured liver epithelium reveals dynamic heterogeneity
- Transcriptional heterogeneity is driven by fluctuating activation of YAP signaling
- YAP is essential for adult biliary cell survival under homeostatic conditions
- YAP is required in hepatocytes for the ductular response during regeneration

Single-Cell Analysis of the Liver Epithelium Reveals Dynamic Heterogeneity and an Essential Role for YAP in Homeostasis and Regeneration

Brian J. Pepe-Mooney,^{1,2,16} Michael T. Dill,^{1,2,3,16} Anna Alemany,⁴ Jose Ordovas-Montanes,^{5,6,7,8,9} Yuki Matsushita,¹⁰ Anuradha Rao,¹¹ Anushna Sen,¹² Makoto Miyazaki,¹³ Sayeepriyadarshini Anakk,¹² Paul A. Dawson,¹¹ Noriaki Ono,¹⁰ Alex K. Shalek,^{5,6,7,8,9,14} Alexander van Oudenaarden,⁴ and Fernando D. Camargo^{1,2,15,17,*}

¹Stem Cell Program, Boston Children's Hospital, Boston, MA 02115, USA

²Department of Stem Cell and Regenerative Biology, Harvard University, Cambridge, MA 02138, USA

³Department of Pediatrics, Harvard Medical School, Boston, MA 02115, USA

⁴Oncode Institute, Hubrecht Institute-KNAW (Royal Netherlands Academy of Arts and Sciences) and University Medical Center Utrecht, 3584 CT Utrecht, the Netherlands

⁵Institute for Medical Engineering and Science, MIT, Cambridge, MA 02139, USA

⁶Department of Chemistry, MIT, Cambridge, MA 02139, USA

⁷Koch Institute for Integrative Cancer Research, MIT, Cambridge, MA 02142, USA

⁸Ragon Institute of MGH, MIT and Harvard, Cambridge, MA 02139, USA

⁹Broad Institute of Harvard and MIT, Cambridge, MA 02142, USA

¹⁰Department of Orthodontics and Pediatric Dentistry, University of Michigan School of Dentistry, Ann Arbor, MI 48109, USA

¹¹Department of Pediatrics, Emory University School of Medicine, Atlanta, GA 30322, USA

¹²Department of Molecular and Integrative Physiology, University of Illinois at Urbana-Champaign, Urbana, IL 61801, USA

¹³Division of Renal Diseases and Hypertension, Department of Medicine, University of Colorado Denver, Aurora, CO 80045, USA

¹⁴Harvard-MIT Division of Health Sciences & Technology, Cambridge, MA 02139, USA

¹⁵Harvard Stem Cell Institute, Boston, MA 02115, USA

¹⁶These authors contributed equally

¹⁷Lead Contact

*Correspondence: fernando.camargo@childrens.harvard.edu

<https://doi.org/10.1016/j.stem.2019.04.004>

SUMMARY

The liver can substantially regenerate after injury, with both main epithelial cell types, hepatocytes and biliary epithelial cells (BECs), playing important roles in parenchymal regeneration. Beyond metabolic functions, BECs exhibit substantial plasticity and in some contexts can drive hepatic repopulation. Here, we performed single-cell RNA sequencing to examine BEC and hepatocyte heterogeneity during homeostasis and after injury. Instead of evidence for a transcriptionally defined progenitor-like BEC cell, we found significant homeostatic BEC heterogeneity that reflects fluctuating activation of a YAP-dependent program. This transcriptional signature defines a dynamic cellular state during homeostasis and is highly responsive to injury. YAP signaling is induced by physiological bile acids (BAs), required for BEC survival in response to BA exposure, and is necessary for hepatocyte reprogramming into biliary progenitors upon injury. Together, these findings uncover molecular heterogeneity within the ductal epithelium and reveal YAP as a protective rheostat and regenerative regulator in the mammalian liver.

INTRODUCTION

The liver is an indispensable organ with compartmentalized metabolic function and significant regenerative capabilities. While the two main epithelial cell types within the liver, hepatocytes and biliary epithelial cells (BECs), play a vital role in both of these processes, recent work has illuminated a more prominent functional role for BECs. Indeed, while BECs are essential for the modification and transport of toxic canalicular bile (Jones et al., 2015; Tabibian et al., 2013), they also exhibit remarkable plasticity and can even serve as the major cell source for regenerative cellular expansion after damage (Jörs et al., 2015; Rodrigo-Torres et al., 2014; Schaub et al., 2014; Yanger et al., 2014). Furthermore, recent lineage tracing studies have shown that BECs can act as facultative liver stem cells to repopulate the liver parenchyma in fulminant or chronic liver injury (Deng et al., 2018; Huch et al., 2015; Lu et al., 2015; Raven et al., 2017).

Despite the emerging significance of BECs as liver progenitor cells, debate remains as to whether all BECs have regenerative capacity. Studying BEC heterogeneity has proven arduous due to low cell abundance and difficulties with their isolation and purification. As a result, understanding has remained cursory, with subset evaluations restricted to isolation techniques that account for differences in cell size (Kanno et al., 2000) or by *a priori* choices of variably expressed biliary markers, such as ST14 or CD133 (Li et al., 2017; Kamimoto et al., 2016; Kanno et al., 2000; Lu et al., 2015; Okabe et al., 2009). Despite these

advances, a detailed and unbiased approach to understanding heterogeneity of the liver epithelium, in homeostasis and upon regeneration, has yet to be realized.

Here, we utilize high-throughput single-cell RNA sequencing (scRNA-seq) to uncover and dissect the transcriptional heterogeneity of adult homeostatic and injured hepatocytes and BECs. Upon combination, our data uncover a YAP transcriptional module driving dynamic heterogeneity in BECs. Additional lineage tracing and hepatocyte- and BEC-specific *Yap* knockout (KO) mouse models further reveal that YAP in the liver epithelium is an essential transcriptional rheostat regulating the dynamic and regenerative response to environmental stimuli.

RESULTS

scRNA-Seq Analysis Reveals Transcriptional Heterogeneity in the Biliary Epithelium

To probe heterogeneity in an unbiased manner, intrahepatic BECs from adult mice were isolated and purified by fluorescence-activated cell sorting (FACS) using EpCAM, a well-established marker for BECs (Lu et al., 2015), and processed by inDrop (Klein et al., 2015) for scRNA-seq (Figures 1A and S1A). A total of 2,344 BECs from three independent adult mice were analyzed and showed strong transcriptomic overlap by t-distributed stochastic neighbor embedding (t-SNE), as well as similar transcript and gene counts per cell (Figures 1B, S1B, and S1C). Notably, while the common BEC markers *Sox9* and *Epcam* were uniformly highly expressed, several other well-known biliary markers, such as *Krt19*, and *Hnf1 β* , showed variable or low expression levels (Figures 1C and S1D), supporting previously observed differences in labeling or recombination efficiency (Yanger et al., 2013). Previously proposed progenitor markers, such as *Prom1* (Lu et al., 2015), *St14* (Li et al., 2017), and *Foxj1* (Dorrell et al., 2011), did not typify any subpopulation in our clustering analysis (Figure S1E), nor did they show a unique set of shared genes by correlation analysis. While positive correlations with receptor and/or transporter genes commonly known to associate with larger, distal BECs, such as *Cftr* and *Sctr* (SR), revealed other interesting transporters, these did not define a unique BEC subset in the scRNA-seq analysis, and therefore, further evaluation was not pursued (Figure S1F; Table S1). Finally, analysis identified a small subpopulation of cells ($N = 5$), expressing *Dmbt1* and *Ly6d*, suggestive for extrahepatic BECs (De Lisle et al., 1997). Immunofluorescence (IF) stains confirmed these genes to be exclusively expressed extrahepatically (Figures S1G and S1H; Table S2).

While the isolated BECs maintain a generally congruous transcriptional landscape, an unsupervised clustering analysis with RaceID3 revealed that heterogeneity was primarily defined by a set of genes including *Cyr61*, *Ankrd1*, and *Gadd45b* (Figure 1C). Hierarchical clustering of the filtered 286 genes, based on Z-scored expression, revealed two cell groupings separated across t-SNE2 (y axis): subset A (26% of the cells), which express these genes, as opposed to subset B (Figure 1D). Upon examination of the full list of differentially expressed genes between the two populations (Table S3), we recognized many bona fide targets of the central downstream transducer of the Hippo signaling pathway, YAP (Galli et al., 2015; Stein et al., 2015). Performing a Gene Set Enrichment Analysis (GSEA) of our gene list over a

well-established active YAP signature (Dong et al., 2007), we confirmed that these differentially expressed genes were indeed significantly enriched for YAP targets (Figure 1E). Identification of YAP peaks at, or within the vicinity of, promoters of *Cyr61*, *Klf6*, *Ankrd1*, and *Gadd45b* in previously acquired chromatin immunoprecipitation sequencing (ChIP-seq) data from human biliary cells (Galli et al., 2015) further suggests these genes are direct targets of YAP (Figure S2A). Gene ontology (GO) analysis revealed other enriched GO terms, such as mitogen-activated protein kinase (MAPK) signaling, transcription factor AP-1 complex, and mechanical stimulus and/or cell adhesion (Figure 1F), that have been associated with active YAP signaling (Dubois et al., 2016; Reddy and Irvine, 2013; Yang et al., 2016; Zanconato et al., 2015). Taken together, we find that BEC transcriptional heterogeneity in homeostasis is defined by a YAP target gene signature. Previously, YAP has been shown to be critical for BEC maturation during embryonic development (Zhang et al., 2010) and can lead to expansion of ductal-like cells (Benhamouche et al., 2010; Lee et al., 2010; Lu et al., 2010). However, while there is evidence that supports a role for YAP in establishing biliary fate, the role of YAP in ductal heterogeneity and its overall function in adult BECs have not been previously defined.

YAP Transcriptional Activity Distinguishes BEC Heterogeneity and Is Dynamic

To validate heterogeneous YAP activity *in vivo*, we utilized IF as well as RNA single-molecule *in situ* hybridization (RNA-ISH) for *Cyr61*, *Klf6*, and *Hes1*, another gene identified by our scRNA-seq analysis (Figure S1I). Our data demonstrate a range of expression of these genes within individual ducts, including BECs that display an absence of such transcripts (Figure 2A). Significant correlation of gene expression, observed in the scRNA-seq, was confirmed between *Cyr61* and *Klf6* or *Hes1* (Figure 2B). Similarly, IF for JUNB protein and phosphorylated ERK (pERK), a surrogate for active MAPK signaling, highlighted clear intra-ductal molecular heterogeneity and small groupings of cells (two or three cells) with positive signal (Figure 2C). Using a knockin BAC-transgenic YAP-reporter mouse, which expresses EGFP under the control of the *Cyr61* regulatory sequences (*Cyr61*eGFP), we further demonstrated heterogeneous expression *in situ* and by FACS (Figures 2D–2F). We confirmed that this *Cyr61*eGFP reporter mouse is responsive to YAP activity *in vivo* (Figures S2B and S2C).

We next assessed potential functional differences between these cells, similarly to previous studies (Li et al., 2017; Lu et al., 2015), based on whether cells with higher levels of *Cyr61* expression would have higher primary biliary organoid forming capacities, a surrogate for stemness (Huch et al., 2015). *Cyr61*eGFP⁺ BECs showed a minimal enrichment in their propensity to form colonies *in vitro* in comparison to GFP⁻ BECs (Figures S2D and S2E), suggesting that YAP transcriptional activity is not a major determinant of organoid-forming capacity. Interestingly, imaging and FACS analysis of sorted GFP⁻ BECs cultured as organoids revealed dramatic upregulation of GFP expression in culture over time (Figure 2G and S2F). This suggests that the YAP-driven gene signature can be induced in previously YAP-naïve cells, likely for survival in these culture conditions. Taken together, these data imply that the identified biliary YAP gene signature reflects a dynamic cell state as opposed to a specialized cell type.

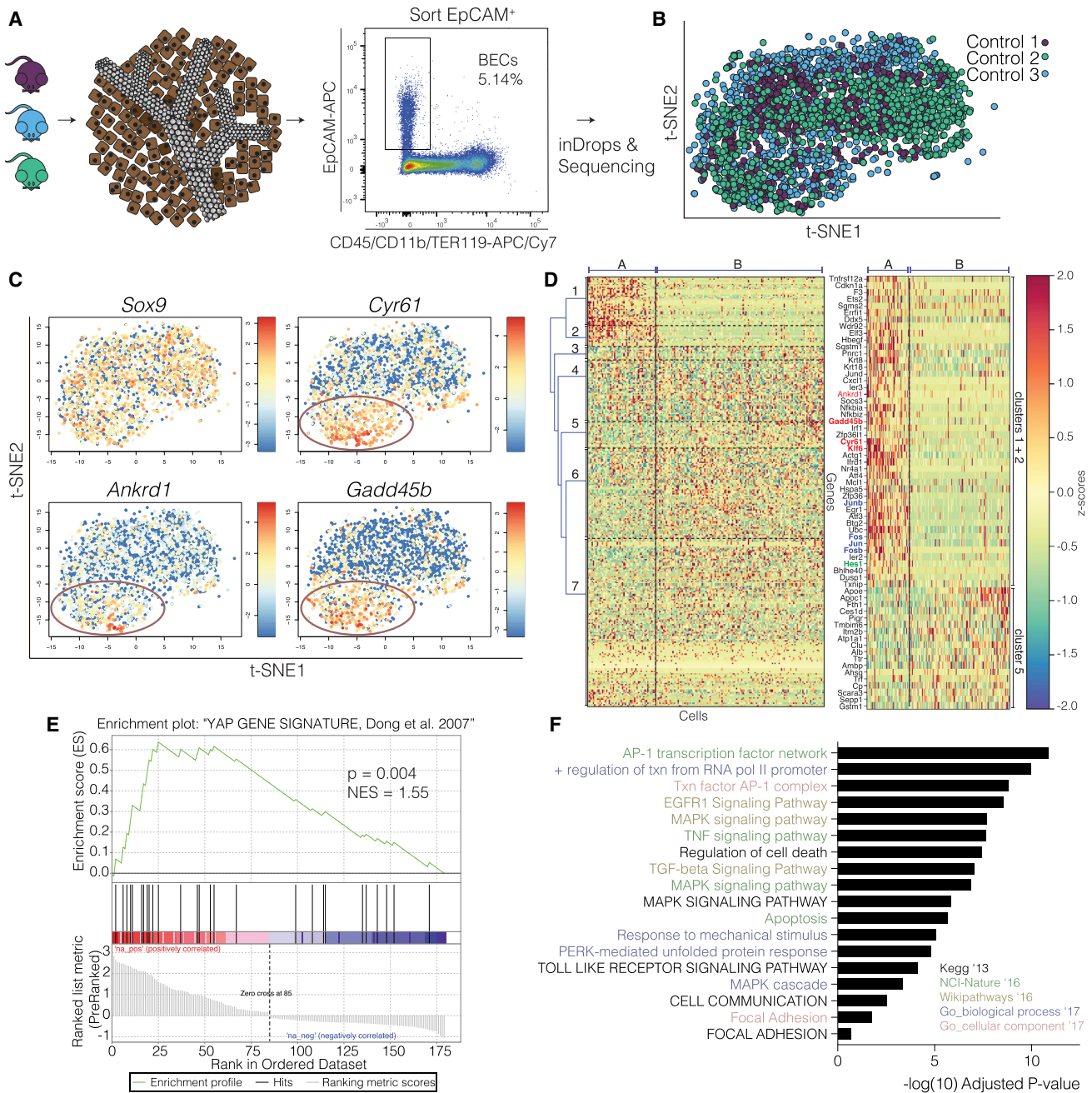


Figure 1. scRNA-Seq Analysis Reveals that Genes Associated with YAP Activity Define Heterogeneity in Adult Homeostatic BECs

(A) Schematic illustrating the isolation procedure for single BECs.
 (B) t-SNE plot of the scRNA-seq data of 2,344 adult BECs (n = 3 mice, indicated with different colors).
 (C) Relative expression of biliary marker *Sox9* and the YAP targets *Cyr61*, *Ankrd1*, and *Gadd45b*, as represented by t-SNE. Colors denote relative expression of the respective gene in each cell (log2). Circles outline cells identified as subset A in (D).
 (D) Heatmap with cells ordered along the x axis (left to right) according to their y axis position (bottom to top) in the t-SNE, and genes on the y axis were hierarchically clustered by their Z scores (with the maximum value set to 3). Right: genes identified from clusters 1, 2, and 5 from the left heatmap. A selection of YAP targets is highlighted in red and AP-1 related genes in blue. Dashed lines separate population of interest (population A) from other BECs (population B).
 (E) GSEA plot of significant differentially expressed genes between populations A and B in comparison to a gene list from YAP overexpression in the liver, indicating enrichment in YAP targets for population A.
 (F) GO analysis of differentially expressed genes between populations A and B using EnrichR, listing terms identified, with bars indicating level of significance. See also Figure S1.

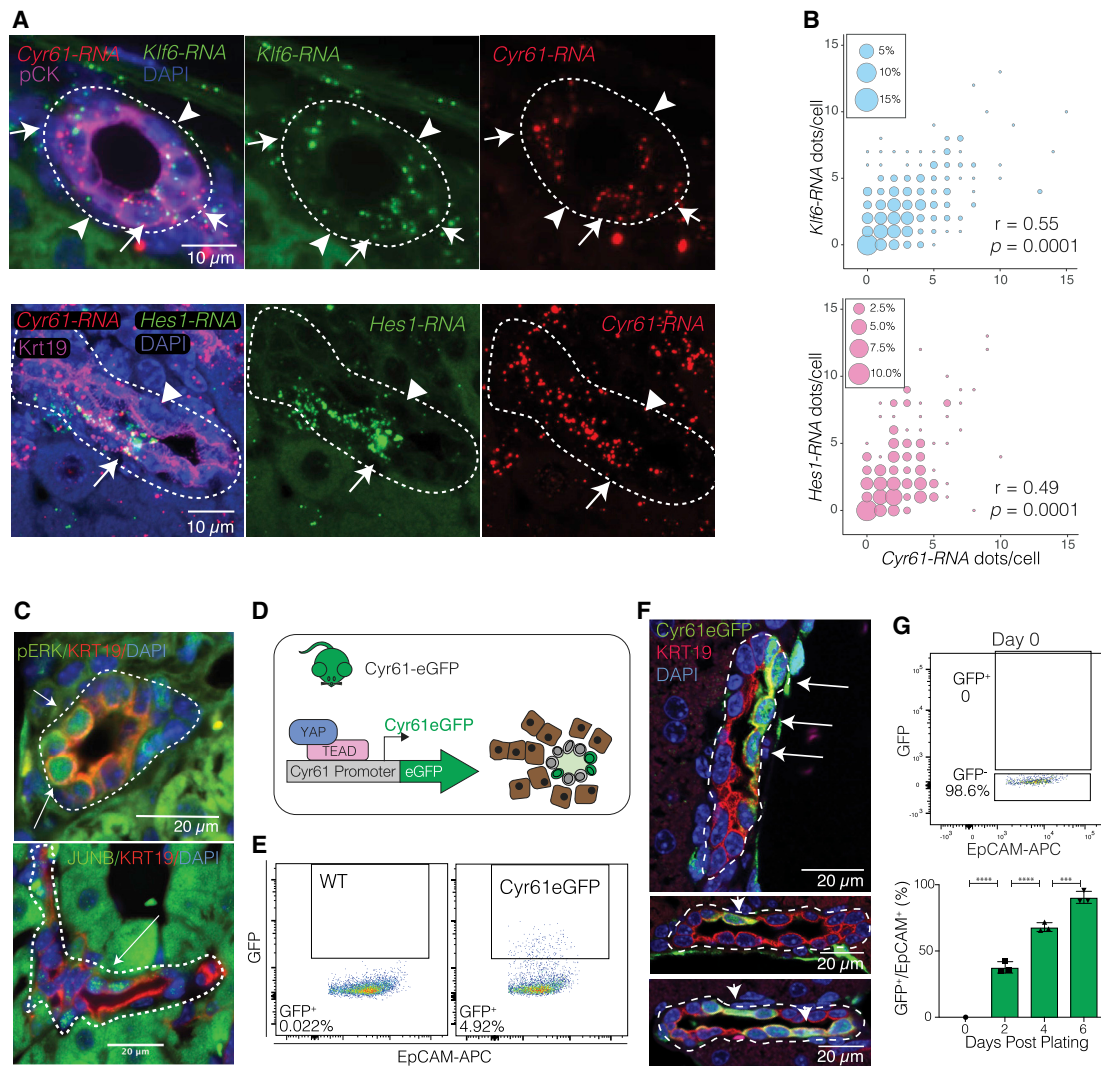


Figure 2. YAP Activity Defines BEC Heterogeneity *In Vivo* and Reflects a Dynamic Cell State *In Vitro*

(A) *Cyr61-Klf6* and *Cyr61-Hes1* RNA-ISH combined with IF stain for pan-cytokeratin (pCK) of mouse liver sections. Arrows indicate BECs co-expressing *Cyr61* and *Klf6* RNA, and arrowheads indicate RNA-negative molecules.

(B) Bubble plots depicting the correlation of co-localized *Cyr61-Klf6* and *Cyr61-Hes1* RNA molecules per BEC. Size of bubble corresponds to the respective co-expression frequency with inset showing size of bubble corresponding to percentage of cells with indicated frequency ($n = 4$ mice, BECs from five portal fields each, Spearman correlation).

(C) IF for pERK and JUNB (arrows) demonstrate heterogeneity within murine cytokeratin19⁺ (KRT19⁺) BECs.

(D) Schematic for the *Cyr61eGFP* transgenic allele, which expresses EGFP under the *Cyr61* promoter and is used as a reporter for YAP transcriptional activity.

(E) Representative FACS analysis of GFP expression in BECs of wild-type (WT) and *Cyr61eGFP* mice, where typically between 3% and 11% GFP⁺ BECs are seen.

(F) IF for GFP-KRT19 demonstrating clear intraductal heterogeneity of expression in the liver of *Cyr61eGFP*-reporter mice. Arrows designate GFP⁺ cells.

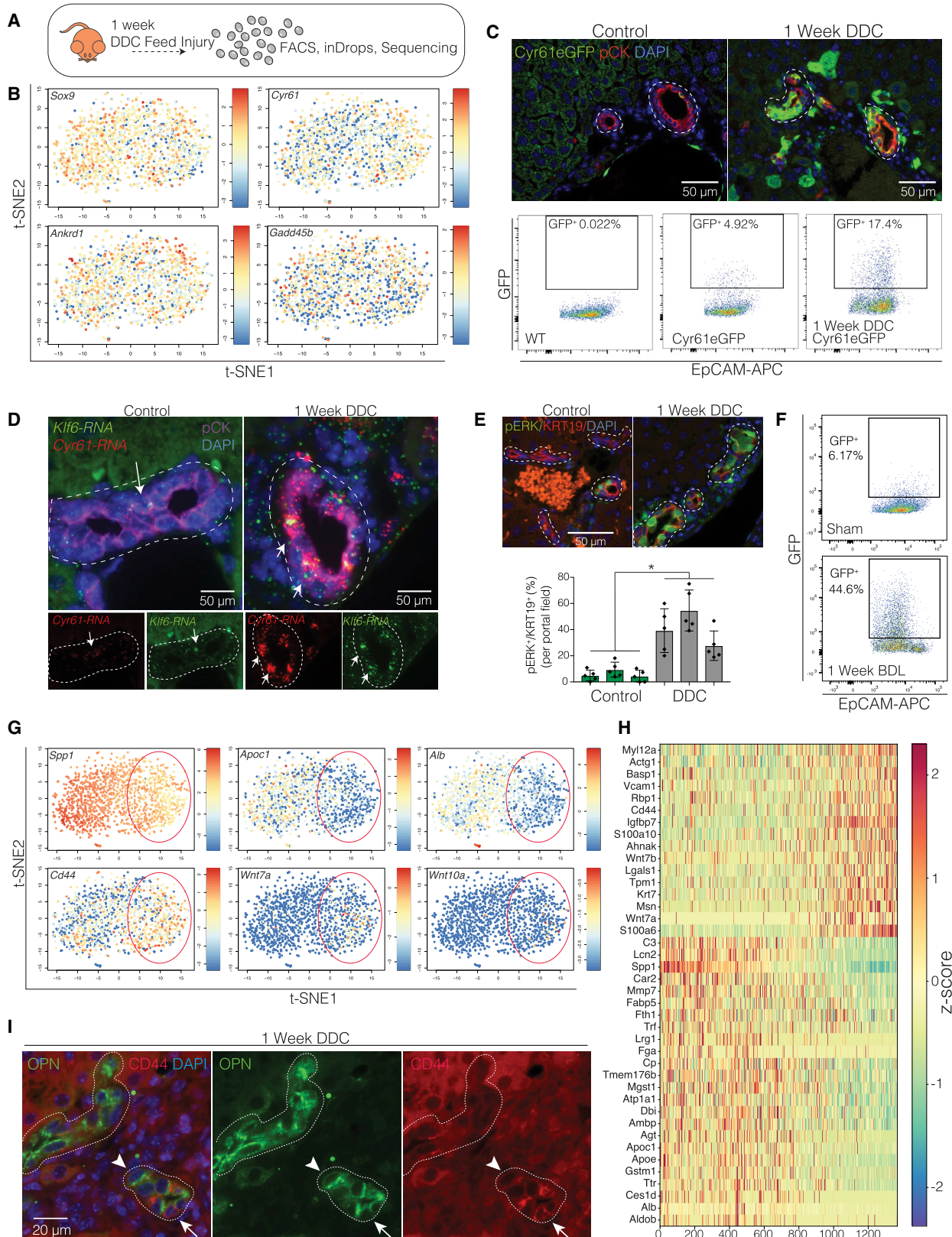
(G) FACS analysis of freshly isolated GFP⁻ BECs sorted from *Cyr61eGFP* mice used for the *in vitro* organoid growth assay. Bar plot depicts percentage of GFP⁺ cells over time, from 5,000 initially seeded GFP⁻ cells, showing that >90% of cultured BECs start expressing GFP within 6 days (mean \pm SD, $n = 3$ mice, each in triplicate, ANOVA, followed by Tukey multiple comparisons test, *** indicate $p < 0.001$, and **** $p < 0.0001$, respectively).

Dashed lines generally outline biliary structures. See also Figure S2.

scRNA-Seq of Regenerating BECs Reveals a Broadened YAP Transcriptional Response and the Compartmentalized Emergence of a Wnt-Associated Signaling Module

To address the heterogeneity of transcriptional changes in response to chronic injury *in vivo*, we next performed scRNA-seq of BECs from mice which had been administered, for 1 week, a diet supplemented with 0.1% 3,5-diethoxycarbonyl-1,4-dihydro-

collidine (DDC) (Kaneko et al., 2015). As expected, DDC injury resulted in increased biliary proliferation as determined by IF for PCNA (Figure S3A). Upon scRNA-seq analysis, 1,268 BECs from a DDC-treated mouse occupied a separate transcriptional space in the t-SNE compared to control BECs (Figures S3B and S3C). This could be well explained by expression changes in a variety of typically upregulated genes, such as *Cxcl2* and *Tacstd2* (Rodrigo-Torres et al., 2014) (Figure S3C; Table S4).



(legend on next page)

Intriguingly, we also determined that the number of YAP-active BECs increased upon DDC administration but no longer occupied a separate spatial location by t-SNE (Figures 3A and 3B). IF for GFP and pERK, FACS analysis of Cyr61eGFP mice, and RNA-ISH for *Cyr61* and *Klf6* all confirmed increased YAP activity in BECs upon DDC injury (Figures 3C–3E). Furthermore, the same changes were also observed in bile duct ligated mice (Figure 3F). These data demonstrate that BECs utilize a YAP transcriptional program to dynamically respond to chronic liver injury *in vivo*. The upregulation of this transcriptional program likely reflects *naïve* BECs undergoing a change of state as opposed to the expansion of a subpopulation of YAP-active cells.

Exclusively in the DDC sample, we also identified a unique subset of BECs with abundant expression of Wnt-related genes: *Wnt7a*, *Wnt7b*, *Wnt10a*, and *Cd44* (Figures 3G and 3H). These genes were previously found to be generally upregulated in injured BECs and were suggested to mark a progenitor-like state (Okabe et al., 2016). Interestingly, the cells expressing this Wnt-associated signaling module also showed an anti-correlative expression pattern with certain mature hepatocyte markers, such as *Apoc1*, *Alb*, and *Ttr*, and also the biliary marker *Spp1* (Figures 3G and 3H). These cells had a distinct transcriptional profile and could be identified, using CD44 as a surrogate marker, in a subset of BECs within intact luminal bile duct structures (Figures 3G–3I). As we were unable to detect *Lgr5* or *Axin2* induction in BECs in DDC treated livers by scRNA-seq or RNA-ISH (data not shown), the activation of these Wnt-related genes appears to be non-canonically regulated, which has been suggested previously (Okabe et al., 2016).

YAP Is Essential in Hepatocytes for the Regenerative Ductular Response to Injury

To investigate if the identified YAP signature was unique in BECs, we performed scRNA-seq analysis on isolated hepatocytes from untreated (5,087 cells) and DDC-injured (2,596 cells) livers using Seq-Well (Gierahn et al., 2017) (Figures S3D–S3F). Our data confirmed previously established hepatic zonation gene differences based on spatial positioning in the hepatic lobule in control hepatocytes (Halpern et al., 2017) (Figures S3G and S3H). Interestingly, while we could not detect homeostatic hepato-

cytes expressing high levels of genes associated with active YAP, a fraction of hepatocytes was found to upregulate *Cyr61* and *Klf6*, as well as the biliary marker *Spp1*, upon 1 week of DDC injury, suggesting the emergence of the YAP transcriptional program in injured hepatocytes as well (Figures 4A and S3I). Strikingly, RNA-ISH for *Cyr61* and *Klf6* showed robust co-localization and increased expression in an average of 9.23% of DDC-injured hepatocytes primarily in the periportal zone compared to controls (Figure 4B). Our results speak to the activation of YAP upon regeneration in a subset of hepatocytes. As shown previously in the literature, a population of hepatocytes can undergo reprogramming to atypical duct cells during multiple types of injury, generating cells thought to have progenitor-like capacities in a process considered to be critical for normal regenerative response (Yanger et al., 2013). To test whether upregulation of the YAP signature in hepatocytes was important for this process, we induced ablation of YAP and concurrent expression of TdTomato (Tom) selectively in hepatocytes using *Yap^{fl/fl}*; *R26^{L^{SL}-TdTomato/+}* mice administered with AAV8-TBG-Cre (ΔYAP^{HEP}) followed by injury (Figures 4C and S3J). We found that loss of YAP specifically in hepatocytes resulted in a significant attenuation of the ductular reaction post DDC, whereas control mice typically showed increased YAP in some periportal hepatocytes (Figures 4D–4F). Additionally, we observed that while lineage-traced hepatocytes can form duct-like structures under prolonged DDC injury, this response was abrogated in mice who had YAP deleted from the hepatic parenchyma (Figures 4G and 4H). Considering the extent of the diminished ductular reaction in ΔYAP^{HEP} mice, additional non-cell-autonomous mechanisms might also be in play. Taken together, we find that activation of a YAP-driven transcriptional program is crucial for the process of liver regeneration after DDC injury and specifically for hepatocyte reprogramming toward a progenitor, biliary-like fate.

YAP Is Required for the Maintenance of Adult Homeostatic BECs

To better understand the specific role of YAP in BECs, we utilized *Yap^{fl/fl}*; *Krt19^{CreER/+}*; *R26^{L^{SL}-TdTomato/+}* (ΔYAP^{BEC}) mice, in which tamoxifen (TAM) administration induces the deletion of *Yap* and

Figure 3. scRNA-Seq Analysis of DDC-Injured BECs Reveals a Broadened YAP-Signaling Response and the Emergence of a Subset of BECs Expressing a Wnt Transcriptional Module *In Vivo*

- (A) Illustration of the experimental design.
 (B) t-SNE plot of BEC scRNA-seq data from a mouse fed DDC for 1 week. Colors denote relative expression of *Sox9* (biliary marker) and the YAP targets *Cyr61*, *Ankrd1*, and *Gadd45b* in each BEC (log2).
 (C) Top: IF for GFP and pCK on liver sections of *Cyr61eGFP* mice fed a regular (control) or DDC diet for 1 week. Bottom: FACS analysis for GFP on sorted BECs from Control or DDC-fed *Cyr61eGFP* mice.
 (D) RNA-ISH for *Cyr61* and *Klf6* on control and DDC-fed mice depicting an upregulation of these transcripts within the same pCK⁺ BECs.
 (E) Top: IF for pERK-KRT19 on livers from control and DDC-fed *Cyr61eGFP* mice. Bottom: scatter-bar plot of quantified pERK⁺ BECs (mean \pm SD for five portal fields with each bar representing a mouse, * indicates $p < 0.05$).
 (F) Representative FACS plots for sorted BECs of *Cyr61eGFP* mice 1 week after sham operation or bile duct ligation indicating a strong increase of GFP⁺ BECs upon cholestatic injury.
 (G) t-SNE plots of BEC scRNA-seq data from a mouse fed DDC for 1 week. Colors denote relative expression of *Spp1*, *Apoc1*, *Alb*, *Cd44*, *Wnt7a*, and *Wnt10a* (log2). Red oval outlines subset of cells with increased expression of Wnt genes.
 (H) Heatmap representing Z scores of gene expression. Cells were ordered on the x axis (left to right) by their position in the x axis of the t-SNE. Depicted genes ($n = 40$) were selected based on their correlation coefficients ($\text{corr} > 0.25$ or $\text{corr} < -0.25$) with *Wnt7a*, *Wnt7b*, *Cd44*, *Spp1*, and *Apoe1* and then hierarchically clustered by Z scores (maximum value 2.3).
 (I) Representative IF for CD44-OPN (*Spp1*) on livers of mice fed DDC for 1 week. Arrows show CD44^{high} OPN^{low} BECs, whereas arrowheads show CD44^{low} OPN^{high} BECs ($n = 3$ mice). Dashed lines generally outline biliary structures. See also Figure S3.

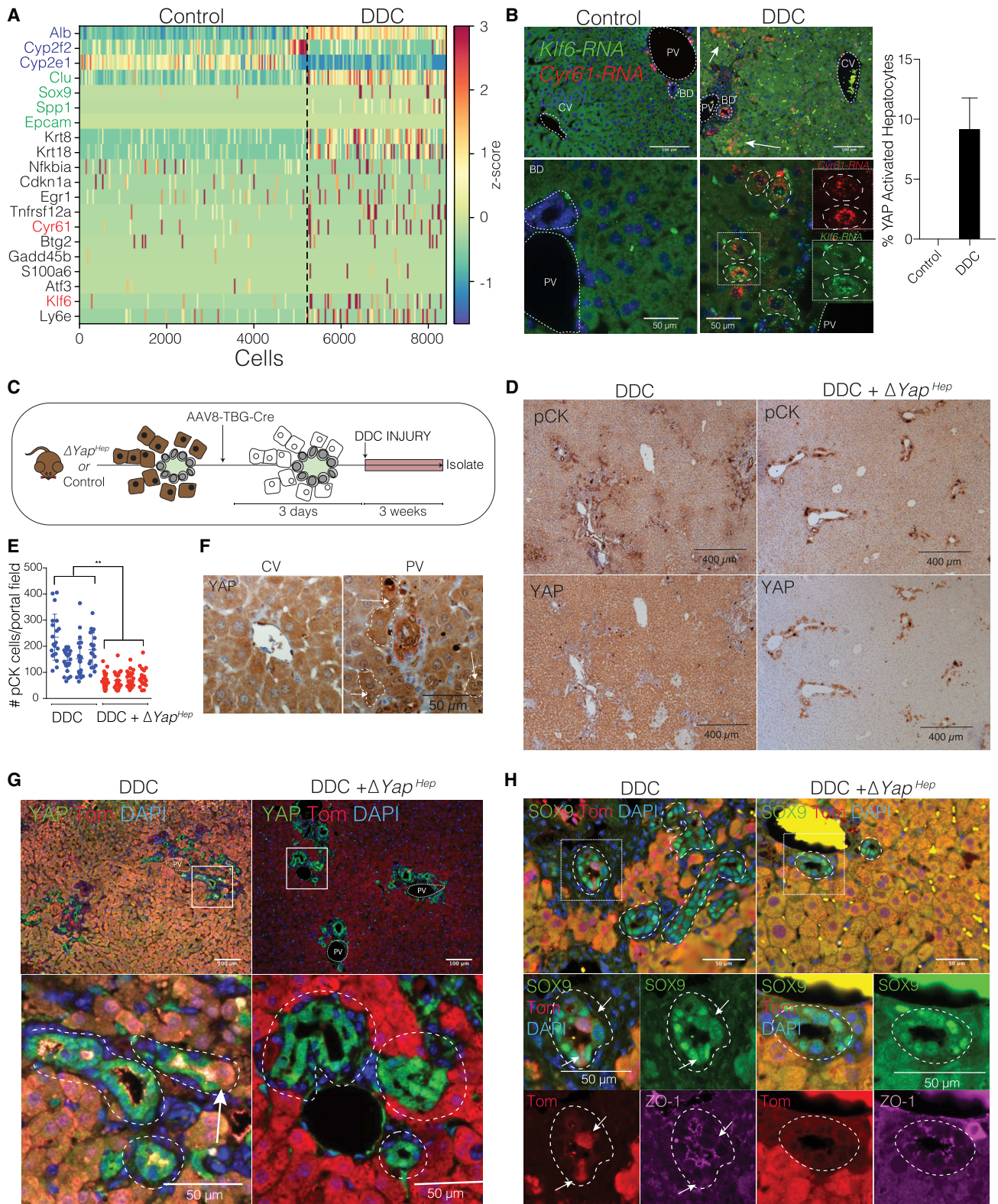


Figure 4. YAP Activity Is Upregulated in a Subset of Hepatocytes and Required for the Hepatocyte Regenerative Ductular Response to Injury
 (A) Heatmap of scRNA-seq analysis of hepatocytes isolated from mice either fed a regular (control) or DDC diet for 1 week, each with cells ordered according to their predicted relative position from the central (left) to the portal vein (right), using landmark genes (exemplary *Alb*, *Cyp2f2*, and *Cyp2e1* in blue). Colors denote relative expression for shown candidate genes (highlighted: biliary markers [green], YAP targets from BECs [black], and RNA-ISH-analyzed genes [red]).

(legend continued on next page)

concurrent expression of Tom in *Krt19*-expressing biliary cells (Means et al., 2008). *Krt19*^{CreER/+}; *R26*^{LSL-TdTomato/+} (Control^{BEC}) mice were used as controls (Figure 5A). Loss of *Yap* was observed in about 40% of BECs 3 days after TAM, which correlated with the percentage of Tom-expressing cells (Figure S4A). Using Tom expression as a surrogate for *Yap* KO, we found a dramatic decrease of Tom⁺ BECs in ΔY_{ap}^{BEC} mice over time compared to a constant labeling percentage in Control^{BEC} mice (Figures 5B and 5C). YAP IF on ΔY_{ap}^{BEC} mice confirmed loss of *Yap* KO cells, while the persistence of YAP⁺ BECs that were also Tom⁺ demonstrated the ability of YAP⁺ escaper BECs to survive (Figures S4B and S4C). Further analysis in ΔY_{ap}^{BEC} mice compared to Control^{BEC} mice, 7 days after TAM, revealed that remaining YAP⁺ BECs in ΔY_{ap}^{BEC} mice proliferate significantly more than control or YAP⁻ BECs (Figure 5D).

As escaper BECs are able to compensate for *Yap* KO-induced BEC loss, in the ΔY_{ap}^{BEC} mouse, we wanted to challenge the biliary epithelium by using *Yap*^{fl/fl}; tetO-Cre; CAG-rTA3 (ΔY_{ap}) mice, which allow for complete, albeit not BEC-specific, KO of *Yap* upon doxycycline (Dox) administration (Figure 5E). In addition to the widespread loss of *Yap* throughout the liver, ΔY_{ap} mice showed extensive disruption of bile duct integrity and morphology with a significant decrease in the number of pCK⁺ cells per portal area 2 weeks after KO (Figures 5F and 5G). Long-term analysis 12 weeks after *Yap* KO revealed dramatic bile duct paucity throughout the entire parenchyma in the ΔY_{ap} livers compared to controls, concurrent with patches of hepatic necrosis and elevated alanine aminotransferase (ALT) and bilirubin levels (Figures 5H, S4D, and S4E). Long-term hepatocyte-specific KO of *Yap* did not result in appreciable changes in morphology or blood chemistry, suggesting against hepatocyte-induced phenotypic effects in the ΔY_{ap} model (Figures S4F and S4G). Surprisingly, while *Yap* deletion efficiency was robust in the entire organism, we did not observe any gross morphological difference upon KO in other solid tissues (Figure S4H). This remarkable observation suggests a unique role for YAP within BECs. Of note, we observed some intact ductal structures, including in the extrahepatic ducts and gallbladder epithelium, at 12 weeks; however, these ducts were YAP⁺, thus highly suggestive of reconstitution of ducts from the few escaper YAP⁺ BECs (Figures S4I and S4J). Taken together, these findings demonstrate that under homeostatic conditions, YAP is acutely and uniquely required for BEC maintenance and the integrity of the liver compared to other tissues in the body.

To identify transcriptional differences, BECs from ΔY_{ap} and control mice were FACS sorted for bulk RNA-seq. Transcriptome analysis revealed 1,426 genes >1.5-fold differentially expressed

(Figure 5I; Table S5) with a mean reduction in normalized *Yap* transcript counts of >90%. Interestingly, among the top enriched downregulated GO terms, we could identify “MAPK signaling” and “focal adhesion,” similar to the scRNA-seq data of the YAP signature subset of BECs in homeostasis (Figures 5J and 1F). As anticipated, downregulation of YAP target genes was also observed upon KO (Figures 5I and S5A–S5C). We also observed almost complete disappearance of pERK in BECs upon *Yap* loss, strengthening the evidence that YAP has effects on MAPK/ERK signaling in adult BECs (Figures S5D and S5E). For upregulated genes upon YAP deletion, the enriched GO terms were mainly associated with inflammation and cell death. Specifically, several pro-apoptotic genes were identified (Figures 5J and S5F), suggesting that the deletion of *Yap* in BECs may lead to cell loss through an apoptotic mechanism. Indeed, IF for cleaved caspase-3, as well as TUNEL analysis, in intrahepatic BECs revealed increased cell death in ΔY_{ap} compared to controls (Figures 5K, 5L, S5G, and S5H). To capture the act of apoptosis in a low-abundant cell type, such as BECs, is particularly challenging, and we posit that as *Yap* loss leads to downregulation of cell adhesion genes, these cells are most likely extruded quickly into the bile. In support of this hypothesis, IF for β -actin reveals the typical basal actin condensing in the process of extrusion (Gu et al., 2011) upon *Yap* KO (Figures S5I and S5J).

Homeostatic YAP Activity in BECs Is Regulated by Bile Acids

The observation that YAP is essential in BECs, even under homeostatic conditions, is particularly remarkable given that YAP is dispensable in several adult homeostatic tissues studied so far (Barry et al., 2013; Chen et al., 2014; Zanconato et al., 2015), and as also suggested from our own initial histological assessment of the ΔY_{ap} mouse (Figure S5E). This notable requirement for YAP, along with the observations that BECs can dynamically upregulate the YAP transcriptional program, led us to the question what might be a unique, causal property of the BEC environment that so distinctly requires YAP. BECs are constantly exposed to bile, containing high levels of hydrophobic bile acids (BAs), such as deoxycholic acid (DCA), which have been shown to be important regulatory molecules and can be toxic in high concentrations (Higuchi et al., 2003). We therefore hypothesized that BA might induce cell toxicity, causing BECs to upregulate the YAP transcriptional program as a protective mechanism. Therefore, we examined the effect of chronically administering DCA-supplemented feed to Cyr61eGFP mice. This resulted in a dramatic increase in the

(B) RNA-ISH for *Klf6* and *Cyr61* in livers of mice fed with regular (control) or DDC diet for 1 week (with magnified insets). Arrows and dashed lines represent YAP-active, periportal hepatocytes that co-express both *Cyr61* and *Klf6* RNA. Bar plot depicts mean \pm SD of YAP-active hepatocytes (n = 3 mice).

(C) Schematic of study design for (D)–(H).

(D) pCK and YAP immunostains of control and ΔY_{ap}^{Hep} mice.

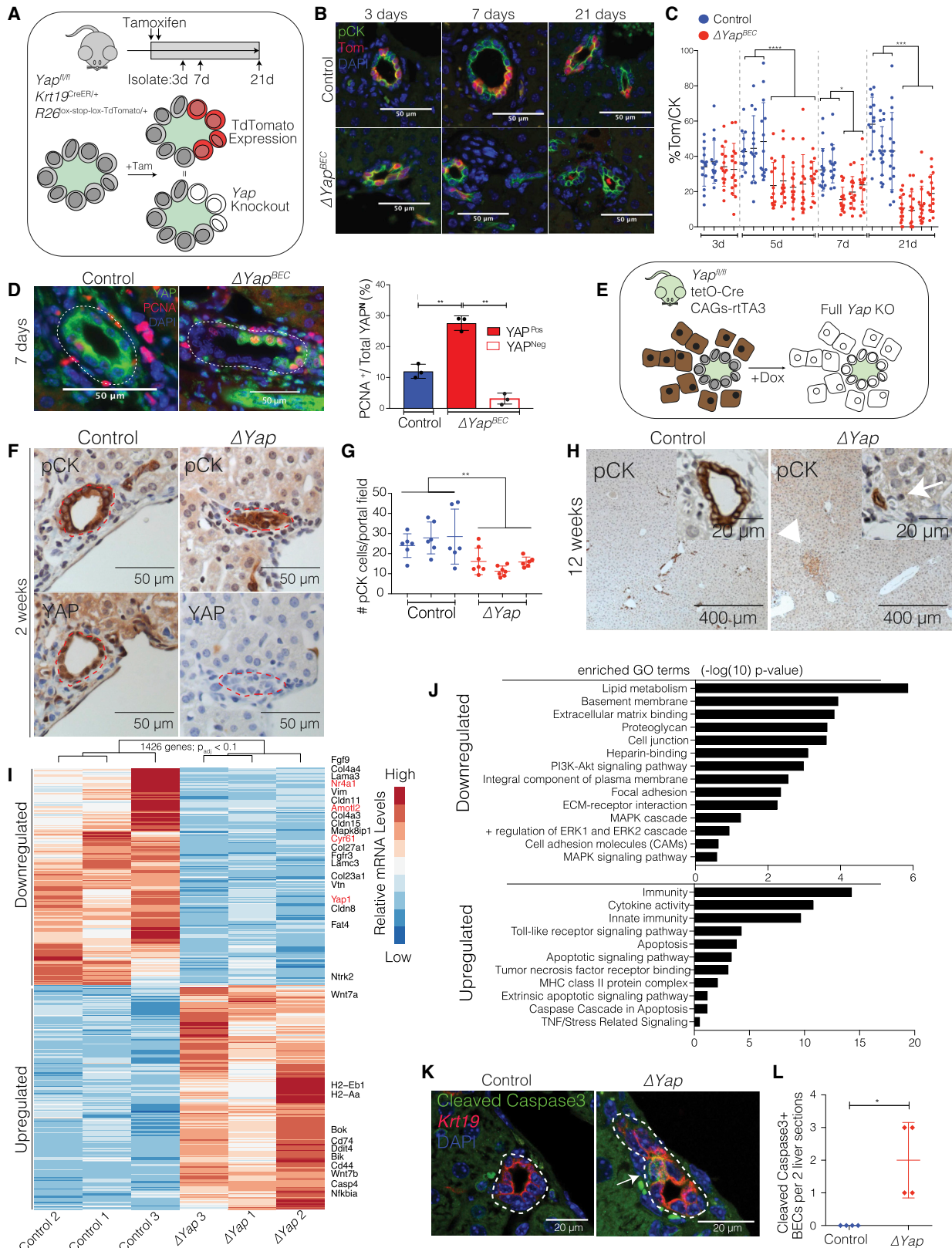
(E) Quantification of pCK⁺ cells per portal field (20 per mouse analyzed, mean \pm SD for each mouse [n = 4], ** indicates p < 0.01).

(F) Representative high-magnification images of YAP immunostain for portal and central vein areas highlighting clusters of YAP^{High} hepatocytes (white dashed lines) that are exclusively periportal. Bile duct is outlined with a red dashed line.

(G) IF for YAP-Tom of control and ΔY_{ap}^{Hep} DDC mice with magnifications. The presence of Tom⁺-KRT19⁺ cells (arrow) is only observed in biliary structures (dashed lines) of control (DDC only) mice (n = 4 mice per group).

(H) IF for SOX9-Tom-ZO-1 of control and ΔY_{ap}^{Hep} DDC mice. Dashed lines outline biliary structures. Magnified insets show SOX9⁺ ducts with apical ZO-1 expression. Arrows indicate SOX9⁺/Tom⁺ cells within the duct exclusively in DDC control mice.

See also Figure S3.



(legend on next page)

number of BECs expressing the YAP transcriptional program (Figures 6A–6F, S6A, and S6B).

We next aimed to determine if the endogenous activity of YAP, perceived in a subset of homeostatic BECs, was correlated with inputs from physiological concentrations of BAs. Hypothesizing that restricting physiological BA exposure would limit active YAP signaling in BECs, *Cyr61eGFP* mice were fed a diet containing 2% of the resin cholestyramine (resin), which is a BA sequestrant (Zhang and Klaassen, 2010), for 1 week. Remarkably, we found that limiting the physiological levels of BAs in mice led to a significant mitigation of the number of BECs expressing the YAP transcriptional program (Figures 6A–6F, S6A, and S6B). We also observed a small number of hepatocytes which co-upregulated *Cyr61* and *Klf6* upon DCA administration, suggesting that a nonphysiological increase in BAs can induce YAP activity in hepatocytes as well (Figure 6G). The gallbladder epithelium, physiologically exposed to very high levels of BAs, did not show an increased induction of YAP activity compared to intrahepatic BECs, suggesting additional protective mechanisms in these cells (Figures S6C and S6D). Together, our findings indicate that physiological BA exposure in intrahepatic BECs is sufficient to activate the YAP-driven transcriptional program.

BA-Induced YAP Activity Is ASBT Dependent and Dynamically Fluctuates in BECs

Our data provide evidence that during homeostasis, only a subpopulation of BECs displays YAP transcriptional activity. Thus, it remains perplexing as to why YAP is required in most, if not all, BECs for survival. We considered the possibility that YAP activity would fluctuate among BECs so that, over a certain time frame, most BECs would have traversed through a YAP activated state. This scenario would explain the observed chronic requirement for YAP in the biliary epithelium. It also would suggest that, if required, most BECs should be able to rapidly turn on YAP transcriptional activity. Indeed, only 24 h after DCA injection, *Cyr61eGFP* expression can be detected in up to 40% of BECs (Figure 7A). To provide further evidence for these transcriptional dynamics, we utilized a lineage-tracing model to label the subset of cells that at a given time displayed YAP transcriptional

activity. As *Hes1* mRNA expression significantly correlated with YAP target genes in YAP-active BECs, we used *Hes1^{CreER/+}; R26^{LSL-TdTomato/+}* reporter mice (Tom^{Hes1}) (Kopinke et al., 2011) (Figure 7B). In support of our initial observations regarding the number of YAP-active BECs, we found that 5 days after TAM, ~13% of BECs were labeled, similar to *Cyr61eGFP* stains (Figures S7A and 6D). We reasoned that if the YAP-active cell state is variable between BECs over time, then a higher overlap of YAP target genes and the Tom label would be observed 1 day after induction when compared to 5 days after. Indeed, RNA-ISH analyses demonstrated a clear correlation between *TdTomato* and *Cyr61* at 1 day post-TAM that was not present after 5 days (Figures 7C and 7D). We interpret this finding as highly supportive of the idea that quiescent BECs dynamically change their YAP activity state over time.

To provide insight into why only a subset of BECs are YAP active at a given time, we next assessed whether the expression of genes involved in regulating BA exposure to BECs, such as mucins or BA transporters, correlate with YAP activity. Although we evaluated several candidates by targeted amplification in our scRNA-seq libraries, we could not identify any significantly correlated genes (Figures S7B and S7C; Table S6). We posited that the lack of transcriptional correlation might be because these genes are regulated post-transcriptionally. To further functionally assess a potential link between YAP activity and several of the main proteins in BA physiology, we decided to evaluate several candidate genes *in vivo*. We focused on (1) TGR5 (also known as *Gpbar1*), a G-protein-coupled receptor known to transmit BA-mediated signaling (Deutschmann et al., 2018); (2) IQGAP1, a scaffolding protein identified to mediate the BA-induced YAP response in hepatocytes (Anakk et al., 2013); and (3) ASBT (also known as *Slc10a2*), a central apical BA transporter in BECs (Lazaridis et al., 1997). Of the three KO mouse models examined, only ASBT showed a significant reduction in the number and distribution of YAP-active BECs during homeostasis, as measured by RNA-ISH for *Cyr61* (Figures 7E, S7D, and S7E). Remarkably, ASBT deficiency drastically abrogated the activation of YAP transcription in BECs following DCA challenge, as compared to controls (Figure 7E).

Figure 5. YAP Is Required for the Maintenance of Adult Homeostatic BECs

- (A) Schematic illustrating experimental design for TAM-inducible biliary-specific *Yap* KO (ΔYAP^{BEC}) and control mice and expected correlation of Tom labeling with *Yap* KO.
- (B) IF for pCK-Tom in ΔYAP^{BEC} and control mice at indicated time points after TAM.
- (C) Scatterplot of the percentage of pCK⁺ BECs that are Tom⁺ at indicated time points after TAM, showing Tom⁺ cell loss in ΔYAP^{BEC} mice over time (mean \pm SD for 15 portal fields per mouse, *** indicate $p < 0.001$, and **** $p < 0.0001$, respectively).
- (D) Left: PCNA and YAP IF on ΔYAP^{BEC} and control mice 7 days after TAM. Right: percentage of PCNA⁺ BECs stratified according to YAP positivity, indicating that KO escaper BECs are actively proliferating (mean \pm SD for 20 portal fields for three mice per group; ANOVA followed by Tukey multiple comparisons test, ** indicates $p < 0.01$).
- (E) Schematic illustrating pan-inducible KO of *Yap* (ΔYap mice).
- (F) Representative serial immunostains of pCK and YAP for ΔYap and control mice 2 weeks after starting Dox, showing efficient *Yap* KO and disintegration of ductal structure in ΔYap mice.
- (G) Scatterplot of the number of pCK cells per portal field in ΔYap and control mice (mean \pm SD for six portal fields per mouse, ** indicates $p < 0.01$).
- (H) Immunostains for pCK of ΔYap and control mice 12 weeks after starting Dox. Arrowhead indicates area of intraparenchymal necrosis. Insets depict bile duct at high magnification, with the arrow indicating a few remaining pCK⁺ cells in ΔYap mice.
- (I) Heatmap of top 1,426 significantly 1.5-fold up- and downregulated genes ($p_{adj} < 0.1$) based on RNA sequencing (RNA-seq) data from FACS-sorted ΔYap and control BECs from mice ($n = 3$ per group) 2 weeks after the start of Dox. YAP-associated genes are highlighted in red.
- (J) GO terms of differentially expressed genes from the DAVID bioinformatics database. Bars indicate level of significance.
- (K) IF for cleaved caspase-3 (cCasp3) from ΔYap and control mice 2 weeks after start of Dox. Arrow points to a positive signal only observed in ΔYap mice.
- (L) Quantification of cCasp3⁺ cells within two histological sections per mouse (mean \pm SD, $n = 4$ mice per group, * indicates $p < 0.05$). Dashed lines generally outline biliary structures. See also Figures S4 and S5.

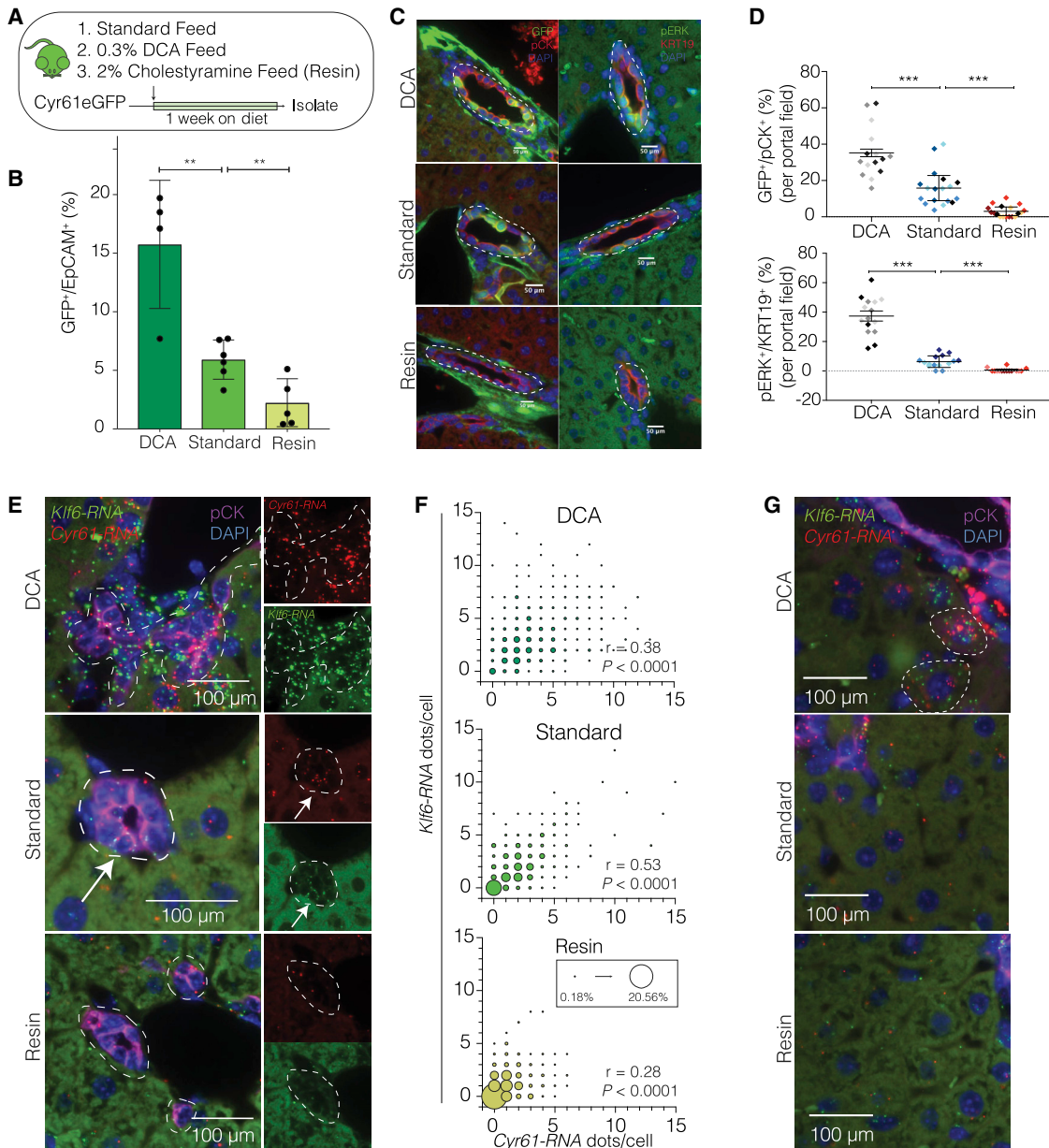


Figure 6. Homeostatic YAP Activity in BECs Is Regulated by BAs

(A) Schematic of the experimental design.

(B) Bar scatterplot of the percentage of GFP⁺ BECs from Cy61eGFP mice on indicated diets by FACS analysis. (Mean ± SD, each dot represents mouse, n = 4–5 per group, ** indicates p < 0.01).

(C) IF for GFP-pCK and pERK/KRT19 in Cy61eGFP mice fed with the indicated diets. Dashed lines outline bile ducts.

(D) Quantification of GFP⁺ (top) and pERK⁺ (bottom) BECs in IF, depicting significant differences between groups. Each color represents an individual mouse per group (Mean ± SD, 5 portal fields per animal, *** indicates p < 0.001).

(E) Dual RNA-ISH for *Cyr61* and *Klf6* with concurrent IF for pCK on Cy61eGFP mice administered the indicated diets. Arrow indicates an exemplary *Cyr61*-*Klf6* co-expressing BEC.

(F) Bubble plots for the quantification of co-localized *Cyr61* and *Klf6* RNA molecules per cell. Size of bubble corresponds to the co-expression frequency for *Cyr61* and *Klf6* within each condition and is indicated as percentage in the inset (n = 4 mice, BECs from five portal fields each; Spearman correlation).

(G) Visualization of the hepatic parenchyma using dual RNA-ISH for *Cyr61* and *Klf6* on mice administered the indicated diets. Dashed lines outline hepatocytes with co-expression in the DCA group.

See also Figure S6.

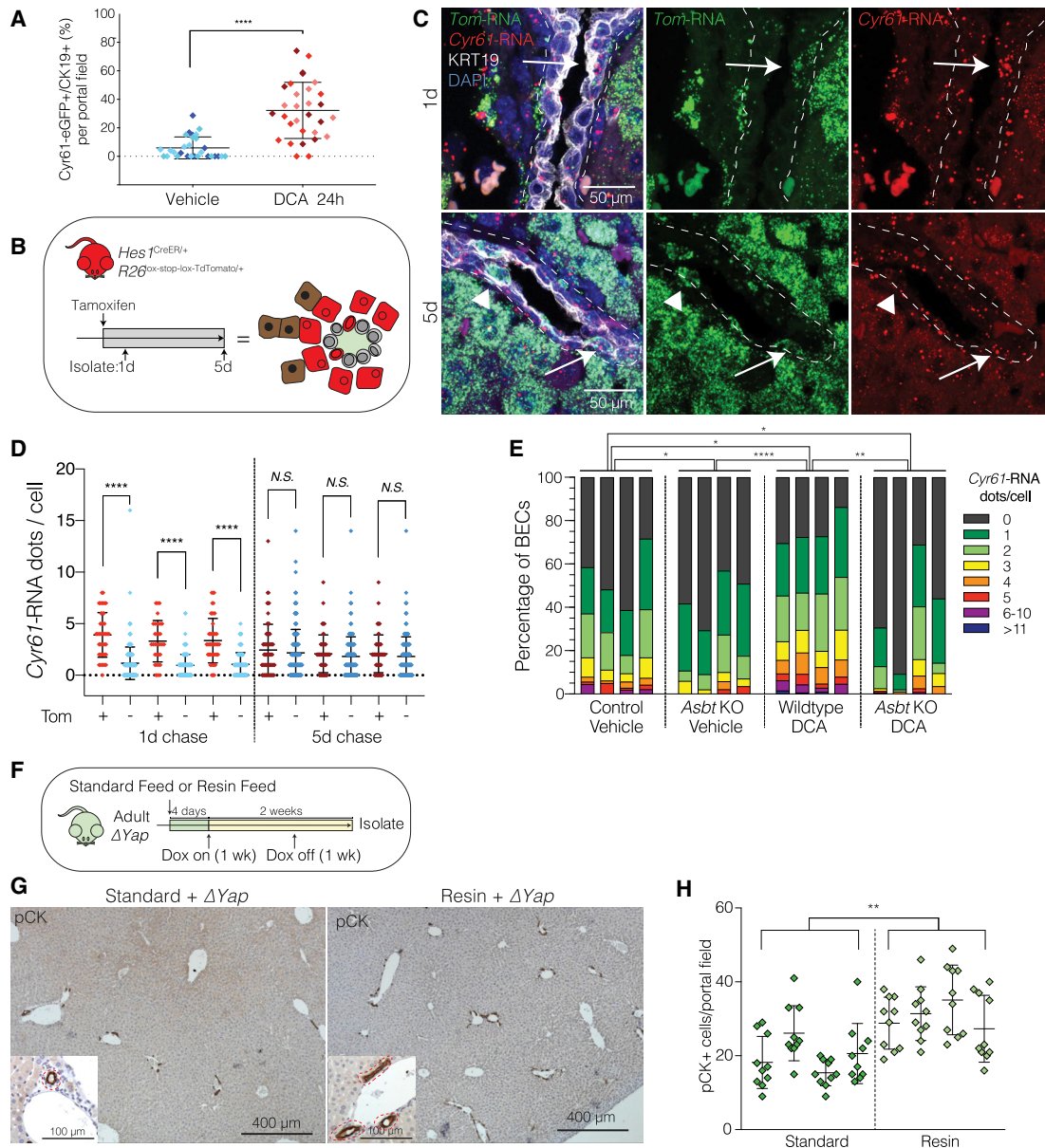


Figure 7. BA-Induced YAP Activity Is ASBT Dependent and Dynamically Fluctuates in BECs Under Physiological Conditions

(A) Scatterplot of the percentage of GFP⁺ BECs per portal field in IF of Cyf61eGFP mouse livers 24 h after intraperitoneal (i.p.) treatment with vehicle or DCA. Each diamond represents a portal field, with colors indicating an individual mouse (Mean ± SD, n = 3 mice per group, **** indicates p < 0.0001).

(B) Schematic illustrating experimental design for TAM-inducible Tom labeling of Hes1-expressing cells with Tom^{Hes1} mice at 1- and 5-day chase for (C) and (D).

(C) Dual RNA-ISH for *Cyr61* and *TdTomato* (*Tom*) with concurrent IF for KRT19 on Tom^{Hes1} mice 1 and 5 days after TAM. Arrows indicate *Tom-Cyr61* co-expressing BECs (enriched in 1-day group), and arrowheads designate exclusively *Tom*-expressing BECs.

(D) Quantification of *Cyr61*-RNA dots per BEC, stratified by Tom positivity, indicating a significant positive correlation only at 1-day chase (Mean ± SD, n = 3 mice per group, **** indicates p < 0.0001).

(E) Distribution bar plot of *Cyr61*-RNA ISH quantification for the indicated groups. Each bar represents a mouse. BECs are color-coded according to the number of *Cyr61*-RNA dots and shown as percentage of cumulative 10 portal fields counted. p values were computed using the Kullback-Leibler test and indicate significant differences between each group (* indicate p < 0.05, ** p < 0.01, and **** p < 0.0001, respectively).

(F) Experimental design.

(G) Low-magnification immunostains for pCK in ΔYap mice fed with indicated diets. Magnified insets depict portal tracts with bile ducts (red dashed lines).

(H) Quantification of pCK⁺ cells per portal field (mean ± SD of 10 portal fields for the indicated mice [n = 4 per group], ** indicates p < 0.01).

See also Figure S7.

These data provide evidence not only that BAs activate YAP signaling in BECs in a direct manner but also that, to do so, they need to be transported intracellularly.

BA Sequestration Rescues Yap-Deletion-Induced BEC Loss

As YAP activity in BECs is regulated by homeostatic levels of BA exposure, this led us to inquire if the phenotype associated with *Yap* KO in BECs might be due to the inability of BECs to respond to BA toxicity through YAP activation. To test this idea, we evaluated whether BA sequestration *in vivo* could partially abrogate the BEC-loss phenotype associated with YAP deletion. Intriguingly, we found that a resin diet almost completely rescued the *Yap* KO phenotype in ΔYap mice. *Yap*-deficient BECs in this diet retained a normal bile duct morphology, and their loss was significantly suppressed (Figures 7F–7H). This finding further supports the important physiological role for YAP as a vital signaling regulator to protect against cell death in BECs.

DISCUSSION

Understanding signaling dynamics and heterogeneity in the liver in homeostasis and regeneration has important implications for advancing treatment of liver disease. As an increasing focus has shifted toward understanding the role of BECs and their regenerative abilities in the liver (Deng et al., 2018; Jörs et al., 2015; Kamimoto et al., 2016; Raven et al., 2017), there has been a vibrant search to identify unique subpopulations of liver cells. Using scRNA-seq, we provide the first unbiased evaluation of the transcriptional landscape of BECs in homeostasis and regeneration. Although we could distinguish rare, transcriptionally distinct, extrahepatic BECs, we were unable to identify a cluster of BECs that could define a potential long-lived stem cell population. Although a limitation of high-throughput scRNA-seq is capture efficiency and sequencing depth per cell, it would seem surprising that a potential progenitor cell would be defined only by a small number of correlated modules comprised of a few low-abundance genes that do not define a distinct cluster of cells in the t-SNE. Our work, instead, uncovers heterogeneity in the biliary epithelium defined by active YAP signaling which can be induced in response to injury or BA exposure *in vivo*. These results discourage the idea of a transcriptionally distinct progenitor-like cell among BECs; rather, they project the hypothesis that these cells have a dynamic ability to respond to environmental cues. The emergence of a subset of BECs expressing Wnt-associated genes upon chronic injury further highlights the plasticity of BECs to respond to environmental signaling inputs.

Regeneration is an essential ability of the liver, which is exposed daily to a multitude of potentially toxic xenobiotics. Several studies have revealed that liver regeneration, typically after partial hepatectomy, does not involve a single pathway but rather engages several different signaling pathways, suggesting redundancy in signaling networks (Michalopoulos, 2010). In chronic liver injury, Yanger et al. (2013) identified Notch signaling as required for hepatocytes to biliary-progenitor cell reprogramming. Our work expands the list of crucially involved pathways, as YAP KO completely inhibits the hepatocytes' re-

programming capacity. As we have previously demonstrated that overexpression of active YAP in hepatocytes drives reprogramming via *Notch2* transcriptional regulation (Yimlamai et al., 2014), the combined evidence is suggestive that YAP-NOTCH is indeed a crucial axis for this process. Interestingly, our single-cell analysis demonstrated that only a fraction of hepatocytes induced YAP activity. Further analyses will be required to determine if these hepatocytes have a predetermined ability to reprogram and if hepatic paracrine factors downstream of YAP influence the ductular reaction by BECs.

In addition to the dynamic response of YAP signaling in the liver epithelium upon injury, the potent BEC loss phenotype observed upon YAP KO is particularly remarkable. Indeed, Hippo signaling had previously appeared to be essential in embryonic development and for injury response but dispensable under homeostatic conditions (Patel et al., 2017). Previous work using an *Mx1^{Cre}* model has suggested that *Yap* KO in the liver without injury does not result in an appreciable phenotype (Bai et al., 2012). Using two different conditional *in vivo* models, however, we show a vital and distinct requirement for YAP in homeostatic BECs. This finding is particularly relevant, as inhibition of YAP has been proposed as a cancer therapeutic strategy (Kim and Myung, 2018; Zanconato et al., 2016). Unless appropriately addressed, hepatotoxicity may therefore become a main limitation to their future use.

Our work resonates with previous observations that YAP and associated pathways are responsive to BAs (Anakk et al., 2013; Centuori et al., 2016) but, in contrast, shows that even physiological levels of BA are sufficient for that response. Interestingly, this BA-triggered YAP activity in BECs seems to dynamically fluctuate between cells. Our short-term BA treatments, coupled with our YAP deletion and *Hes1* lineage tracing data, suggest that most, if not all, homeostatic BECs can and will eventually need to induce YAP activity. Our tracing data reveal that even at 5 days, a different set of BECs express *Hes1-Cyr61*, suggestive of relatively rapid fluctuation. Further studies should provide insight into the timescale of this process, whose dynamics probably explain the lack of consistent correlation between pERK levels and YAP target gene expression in single BECs. Furthermore, we have also identified that ASBT is vital for this transcriptional response, suggesting that the intracellular presence of BA is required. The heterogenic and dynamic transcriptional response in BECs is most likely influenced by a multitude of factors known to alter cellular exposure to BAs, such as the apical glycocalyx, bicarbonate secretion, and the presence of exporting BA transporters, which might cumulatively lower the threshold for a trigger of YAP activity in the individual cell. Additionally, an alternative explanation for the observed heterogeneity is that BECs could become refractory for a certain time to YAP activity. As oscillatory gene expression behaviors have been described in multiple contexts (Bahar Halpern et al., 2015), whether this pattern of YAP activation in BECs is random or follows a defined pattern is unclear and therefore worthy of future exploration.

Our findings add to the nuance, complexity, and variability of YAP signaling depending on environmental conditions and tissue type. For the biliary epithelium, as well as for hepatocytes, this work has determined that YAP signaling is acutely positioned to drive a dynamic response to environmental cues for

continued survival and to regulate regeneration. Further studies evaluating the vital properties of YAP signaling in the liver will lead to a deeper understanding about the nature of our ability to respond to this tempest of environmental toxins and signaling inputs that we encounter daily.

STAR★METHODS

Detailed methods are provided in the online version of this paper and include the following:

- **KEY RESOURCES TABLE**
- **CONTACT FOR REAGENT AND RESOURCE SHARING**
- **EXPERIMENTAL MODEL AND SUBJECT DETAILS**
 - Mice
 - Cell lines
- **METHOD DETAILS**
 - BEC Isolation
 - Fluorescence Activated Cell Sorting
 - BEC Single-Cell RNA Sequencing
 - Targeted Amplification of scRNA-seq library
 - Hepatocyte Isolation
 - Hepatocyte Single-cell RNA-Sequencing
 - Immunohistochemistry / Immunofluorescence
 - RNA *In Situ* Hybridization
 - Microscopy
 - Single-Cell Organoid Forming Assay
 - RNA Isolation and quantitative RT-PCR
 - Bulk RNA-Sequencing
- **QUANTIFICATION AND STATISTICAL ANALYSIS**
 - BEC scRNA-Seq Computational Analysis
 - Hepatocyte scRNA-Seq Computational Analysis
 - Bulk RNA-Sequencing Computational Analysis
 - ChIP-Seq Data Analysis
 - Quantification / Statistical Analysis
- **DATA AVAILABILITY**

SUPPLEMENTAL INFORMATION

Supplemental Information can be found online at <https://doi.org/10.1016/j.stem.2019.04.004>.

ACKNOWLEDGMENTS

The authors are grateful to Ronald Mathieu and Mahnaz Paktinat for assistance with FACS and Luigi Terracciano for his assistance in evaluation of histopathology. The authors thank Charles Murtaugh for Hes1^{CreER} mice and the members of the Camargo laboratory for helpful discussion. This work was supported by a National Science Foundation Predoctoral Award and NIH grant F31 DK107049-01A1 (B.J.P.-M.); Swiss National Science Foundation fellowships P2BSP3_161941 and P300PB_171568 and the Eugen and Elisabeth Schellenberg-Stiftung (M.T.D.); European Research Council Advanced grant ERC-AdG 742225-IntScOmics; Nederlandse Organisatie voor Wetenschappelijk Onderzoek TOP award NWO-CW 714.016.001; and the Foundation for Fundamental Research on Matter, financially supported by the NWO (FOM-14NOISE01) (A.v.O.). A.K.S. was supported by the Searle Scholars Program, the Beckman Young Investigator Program, the Alfred P. Sloan Foundation, the NIH (grants 1DP2GM119419, 2U19AI089992, 1U54CA217377, 2P01AI039671, 5U24AI118672, 2RM1HG006193, and 1R33CA202820), and the Bill and Melinda Gates Foundation (grants OPP1139972 and BMGF OPP1116944). J.O.M. is an HHMI Damon Runyon Cancer Research Foundation Fellow (DRG-2274-16). A.R. and P.A.D. were supported by NIH grant R01

DK047987. Further support was provided by NIH grants R01 DK099559 and NIHR01 AR064036 (F.D.C.).

AUTHOR CONTRIBUTIONS

B.J.P.-M. and F.D.C. conceived the study; B.J.P.-M. and M.T.D. designed, performed, and analyzed experiments and prepared figures; A.A. aided in single-cell figure generation and performed all scRNA-seq computational analysis and additional statistical analysis with direction from B.J.P.-M. and M.T.D. under the supervision of A.v.O.; J.O.-M. performed “Seq-Well” hepatocyte capture, library preparation, and sequencing and pre-processed sequencing data under the supervision of A.K.S.; Y.M., A.R., and A.S. performed experiments on collaborative mouse models under the supervision of N.O., P.A.D., and S.A.; and M.M. performed experiments on collaborative mouse models. F.D.C. supervised the study. B.J.P.-M. and M.T.D. wrote the manuscript, which was edited by all co-authors.

DECLARATION OF INTERESTS

The authors declare no competing interests.

Received: June 27, 2018

Revised: February 4, 2019

Accepted: April 4, 2019

Published: May 9, 2019

REFERENCES

- Anakk, S., Bhosale, M., Schmidt, V.A., Johnson, R.L., Finegold, M.J., and Moore, D.D. (2013). Bile acids activate YAP to promote liver carcinogenesis. *Cell Rep.* 5, 1060–1069.
- Bahar Halpern, K., Tanami, S., Landen, S., Chapal, M., Szlak, L., Hutzler, A., Nizhberg, A., and Itzkovitz, S. (2015). Bursty gene expression in the intact mammalian liver. *Mol. Cell* 58, 147–156.
- Bai, H., Zhang, N., Xu, Y., Chen, Q., Khan, M., Potter, J.J., Nayar, S.K., Cornish, T., Alpini, G., Bronk, S., et al. (2012). Yes-associated protein regulates the hepatic response after bile duct ligation. *Hepatology* 56, 1097–1107.
- Barry, E.R., Morikawa, T., Butler, B.L., Shrestha, K., de la Rosa, R., Yan, K.S., Fuchs, C.S., Magness, S.T., Smits, R., Ogino, S., et al. (2013). Restriction of intestinal stem cell expansion and the regenerative response by YAP. *Nature* 493, 106–110.
- Benhamouche, S., Curto, M., Saotome, I., Gladden, A.B., Liu, C.H., Giovannini, M., and McClatchey, A.I. (2010). Nf2/Merlin controls progenitor homeostasis and tumorigenesis in the liver. *Genes Dev.* 24, 1718–1730.
- Centuori, S.M., Gomes, C.J., Trujillo, J., Borg, J., Brownlee, J., Putnam, C.W., and Martinez, J.D. (2016). Deoxycholic acid mediates non-canonical EGFR-MAPK activation through the induction of calcium signaling in colon cancer cells. *Biochim. Biophys. Acta* 1861, 663–670.
- Chen, E.Y., Tan, C.M., Kou, Y., Duan, Q., Wang, Z., Meirelles, G.V., Clark, N.R., and Ma’ayan, A. (2013). Enrichr: interactive and collaborative HTML5 gene list enrichment analysis tool. *BMC Bioinformatics* 14, 128.
- Chen, Q., Zhang, N., Gray, R.S., Li, H., Ewald, A.J., Zahnow, C.A., and Pan, D. (2014). A temporal requirement for Hippo signaling in mammary gland differentiation, growth, and tumorigenesis. *Genes Dev.* 28, 432–437.
- Dawson, P.A., Haywood, J., Craddock, A.L., Wilson, M., Tietjen, M., Kluckman, K., Maeda, N., and Parks, J.S. (2003). Targeted deletion of the ileal bile acid transporter eliminates enterohepatic cycling of bile acids in mice. *J. Biol. Chem.* 278, 33920–33927.
- De Lisle, R.C., Pettit, M., Huff, J., Isom, K.S., and Agbas, A. (1997). MUCLIN expression in the cystic fibrosis transmembrane conductance regulator knockout mouse. *Gastroenterology* 113, 521–532.
- Deng, X., Zhang, X., Li, W., Feng, R.-X., Li, L., Yi, G.-R., Zhang, X.-N., Yin, C., Yu, H.-Y., Zhang, J.-P., et al. (2018). Chronic liver injury induces conversion of biliary epithelial cells into hepatocytes. *Cell Stem Cell* 23, 114–122.e3.

- Deutschmann, K., Reich, M., Klindt, C., Dröge, C., Spomer, L., Häussinger, D., and Keitel, V. (2018). Bile acid receptors in the biliary tree: TGR5 in physiology and disease. *Biochim Biophys Acta Mol Basis Dis* 1864 (4 Pt B), 1319–1325.
- Dong, J., Feldmann, G., Huang, J., Wu, S., Zhang, N., Comerford, S.A., Gayyed, M.F., Anders, R.A., Maitra, A., and Pan, D. (2007). Elucidation of a universal size-control mechanism in *Drosophila* and mammals. *Cell* 130, 1120–1133.
- Dorrell, C., Erker, L., Lanxon-Cookson, K.M., Abraham, S.L., Victoroff, T., Ro, S., Canaday, P.S., Streeter, P.R., and Grompe, M. (2008). Surface markers for the murine oval cell response. *Hepatology* 48, 1282–1291.
- Dorrell, C., Erker, L., Schug, J., Kopp, J.L., Canaday, P.S., Fox, A.J., Smirnova, O., Duncan, A.W., Finegold, M.J., Sander, M., et al. (2011). Prospective isolation of a bipotential clonogenic liver progenitor cell in adult mice. *Genes Dev.* 25, 1193–1203.
- Dubois, F., Keller, M., Calvayrac, O., Soncin, F., Hoa, L., Hergovich, A., Parrini, M.-C., Mazières, J., Vaisse-Lesteven, M., Camonis, J., et al. (2016). RASSF1A suppresses the invasion and metastatic potential of human non-small cell lung cancer cells by inhibiting YAP activation through the GEF-H1/RhoB pathway. *Cancer Res.* 76, 1627–1640.
- Galli, G.G., Carrara, M., Yuan, W.-C., Valdes-Quezada, C., Gurung, B., Pepe-Mooney, B., Zhang, T., Geeven, G., Gray, N.S., de Laat, W., et al. (2015). YAP drives growth by controlling transcriptional pause release from dynamic enhancers. *Mol. Cell* 60, 328–337.
- Gierahn, T.M., Wadsworth, M.H., 2nd, Hughes, T.K., Bryson, B.D., Butler, A., Satija, R., Fortune, S., Love, J.C., and Shalek, A.K. (2017). Seq-Well: portable, low-cost RNA sequencing of single cells at high throughput. *Nat. Methods* 14, 395–398.
- Grün, D., Muraro, M.J., Boisset, J.-C., Wiebrands, K., Lyubimova, A., Dharmadhikari, G., van den Born, M., van Es, J., Jansen, E., Clevers, H., et al. (2016). De novo prediction of stem cell identity using single-cell transcriptome data. *Cell Stem Cell* 19, 266–277.
- Gu, Y., Forostyan, T., Sabbadini, R., and Rosenblatt, J. (2011). Epithelial cell extrusion requires the sphingosine-1-phosphate receptor 2 pathway. *J. Cell Biol.* 193, 667–676.
- Haghverdi, L., Lun, A.T.L., Morgan, M.D., and Marioni, J.C. (2018). Batch effects in single-cell RNA-sequencing data are corrected by matching mutual nearest neighbors. *Nat. Biotechnol.* 36, 421–427.
- Halpern, K.B., Shenav, R., Matcovitch-Natan, O., Tóth, B., Lemze, D., Golan, M., Massasa, E.E., Baydatch, S., Landen, S., Moor, A.E., et al. (2017). Single-cell spatial reconstruction reveals global division of labour in the mammalian liver. *Nature* 542, 352–356.
- Herman, J.S., Sagar, and Grün, D. (2018). FateID infers cell fate bias in multipotent progenitors from single-cell RNA-seq data. *Nat. Methods* 15, 379–386.
- Higuchi, H., Yoon, J.-H., Grambihler, A., Werneburg, N., Bronk, S.F., and Gores, G.J. (2003). Bile acids stimulate cFLIP phosphorylation enhancing TRAIL-mediated apoptosis. *J. Biol. Chem.* 278, 454–461.
- Huang, W., Sherman, B.T., and Lempicki, R.A. (2009). Systematic and integrative analysis of large gene lists using DAVID bioinformatics resources. *Nat. Protoc.* 4, 44–57.
- Huch, M., Gehart, H., van Boxtel, R., Hamer, K., Blokzijl, F., Verstegen, M.M.A., Ellis, E., van Wenum, M., Fuchs, S.A., de Ligt, J., et al. (2015). Long-term culture of genome-stable bipotent stem cells from adult human liver. *Cell* 160, 299–312.
- Jones, H., Alpini, G., and Francis, H. (2015). Bile acid signaling and biliary functions. *Acta Pharm. Sin. B* 5, 123–128.
- Jörs, S., Jeliaskova, P., Ringelhan, M., Thalhammer, J., Dürl, S., Ferrer, J., Sander, M., Heikenwalder, M., Schmid, R.M., Siveke, J.T., and Geisler, F. (2015). Lineage fate of ductular reactions in liver injury and carcinogenesis. *J. Clin. Invest.* 125, 2445–2457.
- Kamimoto, K., Kaneko, K., Kok, C.Y.-Y., Okada, H., Miyajima, A., and Itoh, T. (2016). Heterogeneity and stochastic growth regulation of biliary epithelial cells dictate dynamic epithelial tissue remodeling. *eLife* 5, e15034.
- Kaneko, K., Kamimoto, K., Miyajima, A., and Itoh, T. (2015). Adaptive remodeling of the biliary architecture underlies liver homeostasis. *Hepatology* 61, 2056–2066.
- Kanno, N., LeSage, G., Glaser, S., Alvaro, D., and Alpini, G. (2000). Functional heterogeneity of the intrahepatic biliary epithelium. *Hepatology* 31, 555–561.
- Kim, H.-B., and Myung, S.-J. (2018). Clinical implications of the Hippo-YAP pathway in multiple cancer contexts. *BMB Rep.* 51, 119–125.
- Klein, A.M., Mazutis, L., Akartuna, I., Tallapragada, N., Veres, A., Li, V., Peshkin, L., Weitz, D.A., and Kirschner, M.W. (2015). Droplet barcoding for single-cell transcriptomics applied to embryonic stem cells. *Cell* 161, 1187–1201.
- Kopinke, D., Brailsford, M., Shea, J.E., Leavitt, R., Scaife, C.L., and Murtaugh, L.C. (2011). Lineage tracing reveals the dynamic contribution of Hes1+ cells to the developing and adult pancreas. *Development* 138, 431–441.
- Lazaridis, K.N., Pham, L., Tietz, P., Marinelli, R.A., deGroen, P.C., Levine, S., Dawson, P.A., and LaRusso, N.F. (1997). Rat cholangiocytes absorb bile acids at their apical domain via the ileal sodium-dependent bile acid transporter. *J. Clin. Invest.* 100, 2714–2721.
- Lee, K.-P., Lee, J.-H., Kim, T.-S., Kim, T.-H., Park, H.-D., Byun, J.-S., Kim, M.-C., Jeong, W.-I., Calvisi, D.F., Kim, J.-M., and Lim, D.S. (2010). The Hippo-Salvador pathway restrains hepatic oval cell proliferation, liver size, and liver tumorigenesis. *Proc. Natl. Acad. Sci. USA* 107, 8248–8253.
- Li, S., Wang, Q., Chakladar, A., Bronson, R.T., and Bernards, A. (2000). Gastric hyperplasia in mice lacking the putative Cdc42 effector IQGAP1. *Mol. Cell Biol.* 20, 697–701.
- Li, W.-C., Ralphs, K.L., and Tosh, D. (2010). Isolation and culture of adult mouse hepatocytes. *Methods Mol. Biol.* 633, 185–196.
- Li, B., Dorrell, C., Canaday, P.S., Pelz, C., Haft, A., Finegold, M., and Grompe, M. (2017). Adult Mouse Liver Contains Two Distinct Populations of Cholangiocytes. *Stem Cell Reports* 9, 478–489.
- Lu, L., Li, Y., Kim, S.M., Bossuyt, W., Liu, P., Qiu, Q., Wang, Y., Halder, G., Finegold, M.J., Lee, J.S., and Johnson, R.L. (2010). Hippo signaling is a potent in vivo growth and tumor suppressor pathway in the mammalian liver. *Proc. Natl. Acad. Sci. USA* 107, 1437–1442.
- Lu, W.-Y., Bird, T.G., Boulter, L., Tsuchiya, A., Cole, A.M., Hay, T., Guest, R.V., Wojtacha, D., Man, T.Y., Mackinnon, A., et al. (2015). Hepatic progenitor cells of biliary origin with liver repopulation capacity. *Nat. Cell Biol.* 17, 971–983.
- Macosko, E.Z., Basu, A., Satija, R., Nemes, J., Shekhar, K., Goldman, M., Tirosh, I., Bialas, A.R., Kamitaki, N., Martersteck, E.M., et al. (2015). Highly parallel genome-wide expression profiling of individual cells using nanoliter droplets. *Cell* 161, 1202–1214.
- Maglic, D., Schlegelmilch, K., Dost, A.F., Panero, R., Dill, M.T., Calogero, R.A., and Camargo, F.D. (2018). YAP-TEAD signaling promotes basal cell carcinoma development via a c-JUN/AP1 axis. *EMBO J.* 37, e98642.
- Means, A.L., Xu, Y., Zhao, A., Ray, K.C., and Gu, G. (2008). A CK19(CreERT) knockin mouse line allows for conditional DNA recombination in epithelial cells in multiple endodermal organs. *Genesis* 46, 318–323.
- Michalopoulos, G.K. (2010). Liver regeneration after partial hepatectomy: critical analysis of mechanistic dilemmas. *Am. J. Pathol.* 176, 2–13.
- Miyoshi, H., and Stappenbeck, T.S. (2013). In vitro expansion and genetic modification of gastrointestinal stem cells in spheroid culture. *Nat. Protoc.* 8, 2471–2482.
- Okabe, M., Tsukahara, Y., Tanaka, M., Suzuki, K., Saito, S., Kamiya, Y., Tsujimura, T., Nakamura, K., and Miyajima, A. (2009). Potential hepatic stem cells reside in EpCAM+ cells of normal and injured mouse liver. *Development* 136, 1951–1960.
- Okabe, H., Yang, J., Sylakowski, K., Yovchev, M., Miyagawa, Y., Nagarajan, S., Chikina, M., Thompson, M., Oertel, M., Baba, H., et al. (2016). Wnt signaling regulates hepatobiliary repair following cholestatic liver injury in mice. *Hepatology* 64, 1652–1666.
- Paolini, M., Pozzetti, L., Montagnani, M., Potenza, G., Sabatini, L., Antelli, A., Cantelli-Forti, G., and Roda, A. (2002). Ursodeoxycholic acid (UDCA) prevents DCA effects on male mouse liver via up-regulation of CYP [correction of CXP] and preservation of BSEP activities. *Hepatology* 36, 305–314.

- Patel, S.H., Camargo, F.D., and Yimlamai, D. (2017). Hippo signaling in the liver regulates organ size, cell fate, and carcinogenesis. *Gastroenterology* *152*, 533–545.
- Raven, A., Lu, W.-Y., Man, T.Y., Ferreira-Gonzalez, S., O'Duibhir, E., Dwyer, B.J., Thomson, J.P., Meehan, R.R., Bogorad, R., Kotliansky, V., et al. (2017). Cholangiocytes act as facultative liver stem cells during impaired hepatocyte regeneration. *Nature* *547*, 350–354.
- Reddy, B.V.V.G., and Irvine, K.D. (2013). Regulation of Hippo signaling by EGFR-MAPK signaling through Ajuba family proteins. *Dev. Cell* *24*, 459–471.
- Rodrigo-Torres, D., Affò, S., Coll, M., Morales-Ibanez, O., Millán, C., Blaya, D., Alvarez-Guaita, A., Rentero, C., Lozano, J.J., Maestro, M.A., et al. (2014). The biliary epithelium gives rise to liver progenitor cells. *Hepatology* *60*, 1367–1377.
- Schaub, J.R., Malato, Y., Gormond, C., and Willenbring, H. (2014). Evidence against a stem cell origin of new hepatocytes in a common mouse model of chronic liver injury. *Cell Rep.* *8*, 933–939.
- Schindelin, J., Arganda-Carreras, I., Frise, E., Kaynig, V., Longair, M., Pietzsch, T., Preibisch, S., Rueden, C., Saalfeld, S., Schmid, B., et al. (2012). Fiji: an open-source platform for biological-image analysis. *Nat. Methods* *9*, 676–682.
- Schlegelmilch, K., Mohseni, M., Kirak, O., Pruszk, J., Rodriguez, J.R., Zhou, D., Kreger, B.T., Vasioukhin, V., Avruch, J., Brummelkamp, T.R., and Camargo, F.D. (2011). Yap1 acts downstream of α -catenin to control epidermal proliferation. *Cell* *144*, 782–795.
- Stein, C., Bardet, A.F., Roma, G., Bergling, S., Clay, I., Ruchti, A., Agarinis, C., Schmelzle, T., Bouwmeester, T., Schübeler, D., and Bauer, A. (2015). YAP1 exerts its transcriptional control via TEAD-mediated activation of enhancers. *PLoS Genet.* *11*, e1005465.
- Subramanian, A., Tamayo, P., Mootha, V.K., Mukherjee, S., Ebert, B.L., Gillette, M.A., Paulovich, A., Pomeroy, S.L., Golub, T.R., Lander, E.S., and Mesirov, J.P. (2005). Gene set enrichment analysis: a knowledge-based approach for interpreting genome-wide expression profiles. *Proc. Natl. Acad. Sci. USA* *102*, 15545–15550.
- Tabibian, J.H., Masyuk, A.I., Masyuk, T.V., O'Hara, S.P., and LaRusso, N.F. (2013). Physiology of cholangiocytes. *Compr. Physiol.* *3*, 541–565.
- Tag, C.G., Sauer-Lehnen, S., Weiskirchen, S., Borkham-Kamphorst, E., Tolba, R.H., Tacke, F., and Weiskirchen, R. (2015). Bile duct ligation in mice: induction of inflammatory liver injury and fibrosis by obstructive cholestasis. *J. Vis. Exp.* *96*, e52438.
- Vassileva, G., Golovko, A., Markowitz, L., Abbondanzo, S.J., Zeng, M., Yang, S., Hoos, L., Tetzloff, G., Levitan, D., Murgolo, N.J., et al. (2006). Targeted deletion of Gpbar1 protects mice from cholesterol gallstone formation. *Biochem. J.* *398*, 423–430.
- Yang, K., Wu, Y., Cheng, P., Zhang, J., Yang, C., Pi, B., Ye, Y., You, H., Chen, A., Xu, T., et al. (2016). YAP and ERK mediated mechanical strain-induced cell cycle progression through RhoA and cytoskeletal dynamics in rat growth plate chondrocytes. *J. Orthop. Res.* *34*, 1121–1129.
- Yanger, K., Zong, Y., Maggs, L.R., Shapira, S.N., Maddipati, R., Aiello, N.M., Thung, S.N., Wells, R.G., Greenbaum, L.E., and Stanger, B.Z. (2013). Robust cellular reprogramming occurs spontaneously during liver regeneration. *Genes Dev.* *27*, 719–724.
- Yanger, K., Knigin, D., Zong, Y., Maggs, L., Gu, G., Akiyama, H., Pikarsky, E., and Stanger, B.Z. (2014). Adult hepatocytes are generated by self-duplication rather than stem cell differentiation. *Cell Stem Cell* *15*, 340–349.
- Yimlamai, D., Christodoulou, C., Galli, G.G., Yanger, K., Pepe-Mooney, B., Gurung, B., Shrestha, K., Cahan, P., Stanger, B.Z., and Camargo, F.D. (2014). Hippo pathway activity influences liver cell fate. *Cell* *157*, 1324–1338.
- Zanconato, F., Forcato, M., Battilana, G., Azzolin, L., Quaranta, E., Bodega, B., Rosato, A., Bicciato, S., Cordenonsi, M., and Piccolo, S. (2015). Genome-wide association between YAP/TAZ/TEAD and AP-1 at enhancers drives oncogenic growth. *Nat. Cell Biol.* *17*, 1218–1227.
- Zanconato, F., Cordenonsi, M., and Piccolo, S. (2016). YAP/TAZ at the roots of cancer. *Cancer Cell* *29*, 783–803.
- Zhang, Y., and Klaassen, C.D. (2010). Effects of feeding bile acids and a bile acid sequestrant on hepatic bile acid composition in mice. *J. Lipid Res.* *51*, 3230–3242.
- Zhang, N., Bai, H., David, K.K., Dong, J., Zheng, Y., Cai, J., Giovannini, M., Liu, P., Anders, R.A., and Pan, D. (2010). The Merlin/NF2 tumor suppressor functions through the YAP oncoprotein to regulate tissue homeostasis in mammals. *Dev. Cell* *19*, 27–38.
- Zilionis, R., Nainys, J., Veres, A., Savova, V., Zemmour, D., Klein, A.M., and Mazutis, L. (2017). Single-cell barcoding and sequencing using droplet microfluidics. *Nat. Protoc.* *12*, 44–73.

STAR★METHODS

KEY RESOURCES TABLE

REAGENT or RESOURCE	SOURCE	IDENTIFIER
Antibodies		
Rat anti-mouse CD326 (EpCAM)-APC (1:100)	BioLegend	Cat#118214; RRID:AB_1134102
Rat anti-mouse CD45-APC/Cy7 (1:100)	BD Biosciences	Cat#557659; RRID:AB_396774
Rat anti-CD11b-APC/Cy7 (1:100)	BD Biosciences	Cat#557657; RRID:AB_396772
Rat anti-mouse TER-119-APC/Cy7 (1:100)	BioLegend	Cat#116223; RRID:AB_2137788
Rabbit anti-LY6D (1:200)	Proteintech	Cat#17361-1-AP; RRID:N/A
Rabbit anti-DMBT1	Millipore	Cat#ABN256; RRID:N/A
Rabbit anti-YAP (1:400 IHC, 1:200 IF)	Cell Signaling Technology	Cat#14074; RRID:AB_2650491
Rat anti-KRT19 (1:10)	DSHB	Cat#Troma-III; RRID:AB_2133570
Goat anti-GFP (1:400 IHC, 1:200 IF)	Abcam	Cat#ab6673; RRID:AB_305643
Goat anti-mCherry (TdTomato)(1:1000 IHC, 1:500 IF)	Sicgen	Cat#AB0040-200; RRID:AB_2333092
Rabbit anti-pCK (1:1000 IHC, 1:500 IF)	Agilent	Cat#Z0622; RRID:AB_2650434
Rabbit anti-phospho-p44/42 MAPK (pERK) (1:200)	Cell Signaling Technology	Cat#4370; RRID:AB_2315112
Mouse anti-PCNA (1:200)	BioLegend	Cat#307901; RRID:AB_314691
Goat anti-mouse Osteopontin (1:50)	R&D Systems	Cat#AF808; RRID:AB_2194992
Rabbit anti-Cleaved Caspase-3 (1:200)	Cell Signaling Technology	Cat#9664; RRID:AB_2070042
Mouse anti-β-Actin (1:200)	Sigma-Aldrich	Cat#A5316; RRID:AB_476743
Rat anti-mouse CD44 (1:200)	BD Biosciences	Cat#550538; RRID:AB_393732
Rabbit anti-JunB (1:200)	Cell Signaling Technology	Cat#3753; RRID:AB_2130002
Rabbit anti-Sox9 (1:200)	Millipore	Cat#AB5535; RRID:AB_2239761
Mouse anti-Zo-1 (1:200)	Thermo Fisher Scientific	Cat#33-9100; RRID:AB_2533147
Donkey anti-rabbit IgG-AF488 (1:1000)	Thermo Fisher Scientific	Cat#A-21206; RRID:AB_2535792
Donkey anti-rabbit IgG-AF594 (1:1000)	Thermo Fisher Scientific	Cat#A-21207; RRID:AB_141637
Donkey anti-rabbit IgG-AF647 (1:1000)	Thermo Fisher Scientific	Cat#A-31573; RRID:AB_2536183
Donkey anti-goat IgG-AF488 (1:1000)	Thermo Fisher Scientific	Cat#A-32814; RRID:AB_2762838
Donkey anti-goat IgG-AF594 (1:1000)	Thermo Fisher Scientific	Cat#A-11058; RRID:AB_2534105
Donkey anti-mouse IgG-AF488 (1:1000)	Thermo Fisher Scientific	Cat#A-21202; RRID:AB_141607
Donkey anti-mouse IgG-AF594 (1:1000)	Thermo Fisher Scientific	Cat#A-21203; RRID:AB_2535789
Donkey anti-rat IgG-AF488 (1:1000)	Thermo Fisher Scientific	Cat#A-21208; RRID:AB_2535794
Donkey anti-rat IgG-AF594 (1:1000)	Thermo Fisher Scientific	Cat#A-21209; RRID:AB_2535795
Donkey anti-rat IgG-AF647 (1:1000)	Abcam	Cat#ab150155; RRID:N/A
Biotinylated goat anti-rabbit (1:1000)	Vector Laboratories	Cat#BA-1000; RRID:AB_2313606
Biotinylated rabbit anti-goat (1:1000)	Vector Laboratories	Cat#BA-5000; RRID:AB_2336126
Bacterial and Virus Strains		
AAV8.TBG.PI.eGFP.WPRE.bGH	University of Pennsylvania Vector Core	AV-8-PV0146
AAV8.TBG.PI.Cre.rBG	University of Pennsylvania Vector Core	AV-8-PV1091
Chemicals, Peptides, and Recombinant Proteins		
3,5-diethoxycarbonyl-1,4-dihydroxycollidine	Bio-Serv	Cat#S4643
Cholestyramine resin	Sigma-Aldrich	Cat#C4650
Deoxycholic acid	Sigma-Aldrich	Cat#30960
Tamoxifen	Sigma-Aldrich	Cat#T5648
Corn oil	Fisher Science Education	Cat#S25271
Paraformaldehyde Aqueous Solution 16%	Electron Microscopy Sciences	Cat#15711

(Continued on next page)

Continued

REAGENT or RESOURCE	SOURCE	IDENTIFIER
EDTA (0.5M, pH, 8.0), autoclaved	Boston BioProducts	Cat#BM-150-500
HEPES Buffer Solution (1 M)	Invitrogen	Cat#15630-080
HBSS, no calcium, no magnesium	Invitrogen	Cat#14170112
Collagenase Type IV	Invitrogen	Cat#17104019
Accutase	Millipore	Cat#SCR005
0.25% Trypsin-EDTA	Life Technologies	Cat#25200-114
RBC (Red Blood Cell) Lysis Solution	QIAGEN	Cat#158904
Liver digest medium	Thermo Fisher	Cat#17703034
Iodixanol (Optiprep)	Axis-Shield	Cat#1114542
Citric-acid based pH 6.0 Antigen Unmasking Solution	Vector Labs	Cat#H-3300
Donkey Serum	Sigma-Aldrich	Cat#D9663
Tween 20	Sigma-Aldrich	Cat#P9416
Prolong Gold antifade with DAPI	Invitrogen	Cat#P36935
Vectastain Elite ABC-HRP reagent	Vector Laboratories	Cat#PK-7100
Diaminobenzidine-reaction kit	Vector Laboratories	Cat#SK-4100
Harris modified hematoxylin	Fisher Scientific	Cat#SH26-4D
Vectamount	Vector Laboratories	Cat#H-5000
Geltrex	Thermo Fisher Scientific	Cat#A1413302
Advanced Dulbecco's modified Eagle's medium/F12 medium	Invitrogen	Cat#2634-028
Fetal bovine serum (FBS)	GIBCO	Cat#26140079
Penicillin/Streptomycin	Invitrogen	Cat#15140-163
L-Glutamine	Invitrogen	Cat#25030-081
N2-supplement	Invitrogen	Cat#17502048
B27 without vitamin A supplement	Invitrogen	Cat#12587010
Nicotinamide	Sigma-Aldrich	Cat#N0636
Dexamethasone	Sigma-Aldrich	Cat#D4902
Y-27632 (Rho Kinase Inhibitor)	Sigma-Aldrich	Cat#Y0503-5MG
Recombinant murine EGF	R&D Systems	Cat#2028-EG-200
Recombinant murine HGF	Peptotech	Cat#315-23
Primocin	Invivogen	Cat#ant-pm-1
Trypan blue solution 0.4%	Fisher Scientific	Cat#50-751-7527
Trizol Reagent	Life Technologies	Cat#15596018
iScript cDNA Synthesis Kit	Bio-Rad	Cat#1708891BUN
Fast SYBR Green Master Mix	Life Technologies	Cat#4385617
Fast Advanced Taqman Master Mix	Life Technologies	Cat#4444557
GoTaq Green Master Mix	Promega	Cat#M7123
Agencourt AMPure XP beads	Beckman Coulter	Cat#A63881
KAPA HiFi HotStart ReadyMixPCR Kit	KAPA Biosystems	Cat#KK2601
Critical Commercial Assays		
Vetscan VS2 Rotor: Comprehensive Diagnostic Profile	Abaxis	N/A
RNAscope Multiplex Fluorescent Detection kit v2	ACDbio	Cat#323110
TSA Fluorescein Plus Evaluation kit	Perkin Elmer	Cat#NEL741E001KT
TSA Cyanine 3 Plus Evaluation kit	Perkin Elmer	Cat#NEL744E001KT
<i>In Situ</i> Cell Detection Kit, TMR red	Sigma Aldrich	Cat#12156792910
NucleoSpin RNA XS	Macherey-Nagel	Cat#740902.50
AF488 Tyramide SuperBoost Kit	Thermo Fisher Scientific	Cat#B40932
QuBit dsDNA HS assay kit	Thermo Fisher Scientific	Cat#Q32851
NextSeq 500/550 High Output kit v2, 75 cycles	Illumina	Cat#TG-160-2005

(Continued on next page)

Continued

REAGENT or RESOURCE	SOURCE	IDENTIFIER
NextSeq 500/550 Mid Output kit v2.5, 150 cycles	Illumina	Cat#20024904
TruSeq RNA Library Preparation Kit v2, Set B	Illumina	Cat#RS-122-2002
Deposited Data		
ScRNA-seq and bulk RNA-seq data	This paper	GEO: GSE125688
Experimental Models: Cell Lines		
Mouse: L-WRN	ATCC	Cat#CRL-3276; RRID:CVCL_DA06
Experimental Models: Organisms/Strains		
Mouse: <i>Cyr61eGFP</i>	(Maglic et al., 2018)	N/A
Mouse: C57BL/6J	Jackson Laboratories	Cat#JAX:000664; RRID:IMSR_JAX:000664
Mouse: <i>Rosa26^{lox-stop-lox-rtTA/+}; Col1a1^{Teto-YapS127A/+}</i>	(Yimlamai et al., 2014)	N/A
Mouse: <i>Krt19^{tm1(cre/ERT)Ggu/J}</i>	Jackson Laboratories	Cat#JAX:026925; RRID:IMSR_JAX:026925
Mouse: B6.Cg-Gt(ROSA)26Sor ^{tm9(CAG-tdTomato)Hze/J}	Jackson Laboratories	Cat#JAX:007909; RRID:IMSR_JAX:007909
Mouse: <i>Yap^{fl/fl}</i>	(Schlegelmilch et al., 2011)	N/A
Mouse: B6N.FVB(Cg)-Tg(CAG-rtTA3)4288Slowe/J	Jackson Laboratories	Cat#JAX:016532; RRID:IMSR_JAX:016532
Mouse: Tg(tetO-cre)1Jaw/J	Jackson Laboratories	Cat#JAX:006224; RRID:IMSR_JAX:006224
Mouse: <i>Hes1^{CreER/+}</i>	Laboratory of Dr. Charles Murtaugh (Kopinke et al., 2011)	N/A
Mouse: B6.Cg-Gt(ROSA)26Sor ^{tm14(CAG-tdTomato)Hze/J}	Jackson Laboratories	Cat#JAX:007914; RRID:IMSR_JAX:007914
Mouse: <i>Asbt</i> KO	(Dawson et al., 2003)	N/A
Mouse: <i>Tgr5</i> KO	(Vassileva et al., 2006)	N/A
Mouse: <i>Iqgap1</i> KO	(Li et al., 2000)	N/A
Oligonucleotides		
Mm-Cyr61 RNAscope probe C1	ACDbio	Cat#429001
Mm-Cyr61 RNAscope probe C2	ACDbio	Cat#429001-C2
Mm-Klf6 RNAscope probe C1	ACDbio	Cat#426901
Mm-Hes1 RNAscope probe C1	ACDbio	Cat#417701
TdTomato RNAscope probe C1	ACDbio	Cat#317041
Mm-Lgr5 RNAscope probe C1	ACDbio	Cat#312171
Mm-Axin2 RNAscope probe C3	ACDbio	Cat#400331-C3
Primers for targeted scRNA-seq library amplification – see Table S7	This paper	N/A
Primers for qRT-PCR – see Table S7	This paper	N/A
Primers for mouse genotyping – see Table S7	This paper	N/A
Software and Algorithms		
Prism 8 for MacOS	Graphpad	https://www.graphpad.com/scientific-software/prism/
Adobe Illustrator CC	Adobe	https://www.adobe.com/products/illustrator.html
Fiji	(Schindelin et al., 2012)	https://fiji.sc
RStudio	RStudio	https://www.rstudio.com
RacelD3	(Herman et al., 2018)	https://github.com/dgrun/RacelD3_StemID2_package
GSEA 3.0 desktop software	(Subramanian et al., 2005)	http://software.broadinstitute.org/gsea/index.jsp
FlowJo	FlowJo	https://www.flowjo.com

CONTACT FOR REAGENT AND RESOURCE SHARING

Further information and requests for resources and reagents should be directed to and will be fulfilled by the Lead Contact, Fernando Camargo (fernando.camargo@childrens.harvard.edu).

EXPERIMENTAL MODEL AND SUBJECT DETAILS

Mice

All animal protocols and procedures were approved by the respective local animal institutional committees. Mice were housed in specific pathogen-free facilities on a 12h light/dark cycle and were given food and water *ad libitum*. All animals used in this study were 7-12 weeks of age unless otherwise specified and were on a C57BL/6 background, except *Tgr5* KO and their controls (FVB) and *Iqgap1* KO and their controls (129/SVJ); both female and male mice were used for experiments. No influence of sex was observed in any of the performed experiments. Whenever possible, littermates with negative genotypes were used as controls. Only experimentally naive mice were used for experiments. The following mouse lines were utilized or generated:

- (1) Cyr61eGFP BAC-transgenic mice were derived from GENSAT and C57BL/6J were obtained from Jackson laboratories.
- (2) $R26^{\text{lox-stop-lox-rTA/+}}$; $Col1a1^{\text{Teto-YapS127A/+}}$; *Cyr61eGFP* mice were generated by mating *Cyr61eGFP* mice with $R26^{\text{lox-stop-lox-rTA/+}}$; $Col1a1^{\text{Teto-YapS127A/+}}$ mice that were previously described (Yimlamai et al., 2014).
- (3) $Krt19^{\text{CreER/+}}$ mice (Jackson Laboratories) were mated with $R26^{\text{LSL-TdTomato/+}}$ Ai9 mice (Jackson Laboratories) and $Yap^{\text{fl/fl}}$ mice (Schlegelmilch et al., 2011) to obtain $Yap^{\text{fl/fl}}$; $Krt19^{\text{CreER/+}}$; $R26^{\text{LSL-TdTomato/+}}$ (ΔYAP^{BEC}) mice and control $Krt19^{\text{CreER/+}}$; $R26^{\text{LSL-TdTomato/+}}$.
- (4) CAG-rTA3 (Jackson Laboratories) mice were mated with (tetO)7-Cre (Jackson Laboratories) and $Yap^{\text{fl/fl}}$ mice (Schlegelmilch et al., 2011) to obtain the following genotypes $Yap^{\text{fl/fl}}$; tetO-Cre; CAG-rTA3 (ΔYAP) and control $Yap^{\text{fl/fl}}$; tetO-Cre.
- (5) For KO of *Yap* in hepatocytes we generated $Yap^{\text{fl/fl}}$; $R26^{\text{LSL-TdTomato/+}}$ Ai9 (ΔYAP^{HEP}).
- (6) $Hes1^{\text{CreER/+}}$ mice (Kopinke et al., 2011) were mated with $R26^{\text{LSL-TdTomato/+}}$ Ai14 mice (Jackson Laboratories) (Tom^{Hes1}).
- (7) *Asbt*, *Tgr5* and *Iqgap1* KO mice have previously been described (Dawson et al., 2003; Li et al., 2000; Vassileva et al., 2006).

Mouse genotyping was performed with GoTaq Green Master Mix (Promega) using the primers listed in Table S7. For injury models, mice were given feed supplemented with 0.1% 3,5-diethoxycarbonyl-1,4-dihydroxycholellidine (DDC) (Bio-Serv) as previously established (Yanger et al., 2014), for the duration specified. Bile duct ligations were performed on adult mice as described previously (Tag et al., 2015) and controlled with sham-operated mice. Gamma irradiated rodent diet supplemented with 2% cholestyramine (resin) or 0.3% deoxycholic acid (DCA) (purchased from Bio-Serv) was administered to mice as previously described (Zhang and Klaassen, 2010). For 24h BA administration, mice were injected intraperitoneally with 24.4 mg/kg of deoxycholic acid (DCA) in Ethanol (1 ml/kg) once (Paolini et al., 2002). To induce Cre expression in the $Krt19^{\text{CreER}}$ models described above, mice were administered 2 doses of 4mg tamoxifen (TAM) (Sigma-Aldrich) dissolved in corn oil intraperitoneally. Tom^{Hes1} mice were administered 1mg TAM once intraperitoneally. Doxycycline was administered to mice in drinking water at a concentration of 1mg/ml unless otherwise specified. For AAV virus administration, AAV8.TBG.PI.eGFP.WPRE.bGH (University of Pennsylvania Vector Core) and AAV8.TBG.PI.Cre.rBG (University of Pennsylvania Vector Core) were administered via retro-orbital injection at the specified dosages at a volume of 100 μ l. For clinical chemistry analysis, 80 μ l of blood was obtained via capillary retro-orbitally and analyzed utilizing chemistry rotors for Vetscan VS2 (Abaxis).

Cell lines

L-WRN cells were used as described to generate conditioned media for organoid culture (secreting Wnt3a, R-spondin, Noggin) (Miyoshi and Stappenbeck, 2013). Cells were cultured in a humidified 5% CO₂ atmosphere at 37°C.

METHOD DETAILS

BEC Isolation

Optimal isolation of a single-cell suspension of biliary cells was obtained by modifying previously established, two-step liver perfusion protocols (Dorrell et al., 2008; Li et al., 2010). Mice were euthanized, the heart and liver were surgically exposed, and a cannula was immediately inserted through an incision in the right atrium into the suprahepatic vena cava inferior. Mouse livers were then perfused by a pre-warmed (37°C) perfusion buffer (50 mM EDTA, 10 mM HEPES in 1X HBSS [GIBCO]) at an initial flow rate of 3 ml/min for 2.5 minutes, followed by an increase in flow rate to 4 ml/min for an additional 2.5 minutes. This was then followed by perfusion with a pre-warmed (37°C) Collagenase Type IV (150 U/mL; Invitrogen) digestion buffer solution (1.25 mM CaCl₂, 4 mM MgCl₂, 10 mM HEPES in 1x HBSS) for 8-10 minutes at a flow rate of 4 ml/min. For the duration of the two-step liver perfusion, the infrahepatic inferior vena cava was digitally occluded every 30 s for 10 s.

After isolating the liver and surgically removing the gallbladder, the capsule was disrupted and the liver was gently and mechanically agitated to release dissociated single cells. The remaining liver was then subjected to serial digestions in Collagenase Type IV (150 U/mL), Accutase (EMD Millipore), and trypsin (0.25%) for 30 minutes, 30 minutes, and 20 minutes, respectively, at 37°C. Dissociated cells were collected after each step and filtered through a 100 μ m cell strainer, washed, and re-suspended in ice-cold resuspension buffer (2% FBS, 1.25 mM CaCl₂, 4 mM MgCl₂, 10mM HEPES, 5 mM glucose in 1X HBSS). The remaining procedure was at 4°C. Hepatocytes were pelleted by a 30xg spin for 5 minutes and discarded, and the remaining cells in the

supernatant were spun at 300xg for 5 minutes. The pelleted cells were resuspended in 5 mL red blood cell lysis buffer (QIAGEN), treated on ice for 7 mins and washed with 10 mL resuspension buffer at 300xg for 5 minutes. The cells were then re-suspended in cold resuspension buffer for further processing or analysis.

Fluorescence Activated Cell Sorting

BECs were stained by a fluorescent antibody for the positive selection biliary marker EpCAM (Biolegend, 1:100) and negatively selected for by the mesenchymal/hematopoietic lineage markers CD45 (BD Biosciences, 1:100), CD11b (BD Biosciences, 1:100), and TER-119 (Biolegend, 1:100) for 30 minutes at 4°C. After a wash with resuspension buffer at 300xg for minutes, BECs were then sorted or analyzed by FACS utilizing a BD FACSAria II, using the 100 μ m nozzle.

BEC Single-Cell RNA Sequencing

Isolated single BECs were encapsulated, and libraries were generated using inDrop (Zilionis et al., 2017) performed at the Single Cell Core at Harvard Medical School. Approximately 1500 cells were encapsulated for each sample. Libraries were sequenced on an Illumina NextSeq 500 sequencer using a NextSeq 500/500 High Output v2 kit, 75 cycles: 35 cycles for read 1, 6 cycles for index i7 read, and 51 cycles for read 2.

Targeted Amplification of scRNA-seq library

For targeted amplification the post-*in vitro* transcription back-up of the three control BEC scRNA-seq libraries were used with an adaptation of the original inDrop protocol (Zilionis et al., 2017). The samples were directly reverse transcribed according to the protocol but without prior fragmentation and using random hexamers without PE2-adaptor. After clean-up with Agencourt AMPure XP beads at a 1.2X ratio, targeted PCR amplification was performed with 5% of the purified cDNA per each individual reaction using Kapa HiFi Hot Start Mix (KAPA Biosystems) with the respective forward primers and a general reverse primer (Table S7). After clean-up with beads at a 0.8X ratio and evaluation of amplification by gel-electrophoresis, 10 cycles of indexing PCR were performed of the pooled PCR products (15% of the purified PCR product mixed in equal volumes), according to the inDrops protocol. Libraries were sequenced on an Illumina NextSeq 500 sequencer using a NextSeq 500/550 Mid Output v2.5 kit, 150 cycles: 100 cycles for read 1, 8 cycles for index i7 read, 8 cycles for index i5 read, and 14 cycles for read 2.

Hepatocyte Isolation

For hepatocyte isolation, a similar perfusion protocol as described for BEC isolation was used with adaptation of the digestion step, by using liver digest medium (Thermo Fisher) and increasing the digestion time to 16-20 minutes while maintaining identical flow rates. After excision of the liver, the whole procedure was performed at 4°C. The liver capsule removed, and the liver gently swirled in resuspension buffer to yield a cell suspension. After filtration through a 100 μ m cell strainer, the hepatocytes were selectively pelleted by centrifugation with 30xg for 5 minutes, which removes the non-parenchymal cell fraction. The resuspended hepatocytes were then mixed 1:2.2 with 40% iodixanol (Optiprep, Axis-Shield) solution (diluted in resuspension buffer) for a volume of 4.8ml, overlaid with 3 mL 18% iodixanol and 0.5 mL resuspension buffer and spun at 500xg for 25 minutes at 4°C with reduced deceleration. The top cell layer was collected, mixed with resuspension buffer supplemented with 3% BSA and washed once at 30xg for 5 min at 4°C. The cells were then re-suspended in ice-cold resuspension buffer (containing 2% BSA and 9% Optiprep), quantified and assessed for viability by Trypan blue stain. Routinely, viability of over 98% was obtained.

Hepatocyte Single-cell RNA-Sequencing

We utilized the Seq-Well platform for massively parallel scRNA-seq to capture transcriptomes of single hepatocytes on barcoded mRNA capture beads. Full methods on implementation of this platform are available in Gierahn et al. (Gierahn et al., 2017). In brief, 20,000 cells from one *in vivo* hepatocyte condition were loaded onto one array containing 86,000 barcoded mRNA capture beads. The loaded arrays containing cells and beads were then sealed using a polycarbonate membrane with a pore size of 0.01 μ m, which allows for exchange of buffers but retains biological molecules confined within each microwell. Subsequent exchange of buffers allows for cell lysis, transcript hybridization, and bead recovery before performing reverse transcription *en masse*. Following reverse transcription and exonuclease treatment to remove excess primers, PCR amplification was carried out using KAPA HiFi PCR Mastermix with 2,000 beads per 50 μ L reaction volume. Six libraries (totaling 12,000 beads) were then pooled and purified using Agencourt AMPure XP beads by a 0.6X SPRI followed by a 0.7X SPRI and quantified using Qubit hsDNA Assay (Thermo Fisher). Libraries were constructed using the Nextera Tagmentation method on a total of 800 pg of pooled cDNA library from 12,000 recovered beads. Tagmented and amplified sequences were purified at a 0.6X SPRI ratio yielding library sizes with an average distribution of 650-750 base pairs in length as determined using the Agilent hsD1000 Screen Tape System (Agilent Genomics). Arrays were sequenced with an Illumina 75 Cycle NextSeq500/550 High Output v2 kit at a final concentration of 2.8 pM. The read structure was paired end with Read 1 starting from a custom read 1 primer containing 20 bases with a 12bp cell barcode and 8bp unique molecular identifier (UMI) and Read 2 being 50 bases containing transcript information.

Immunohistochemistry / Immunofluorescence

If mice were harvested for BEC isolation, the right-lateral lobe of the liver was ligated and resected before perfusion. If mice were not used for BEC isolation, the whole liver was isolated. Livers and other organs were fixed in 4% Paraformaldehyde for 24-48 hours at

room temperature, washed with PBS and 70% ethanol, and embedded in paraffin. 5 μm sections were rehydrated and treated with citric-acid based pH 6.0 Antigen Unmasking Solution (Vector Labs.) at 95°C in a cooker for 1h for antigen retrieval. Slides were then treated with 0.3% hydrogen peroxide to quench endogenous peroxidase activity. To prevent non-specific antibody binding, slides were incubated in protein blocking solution (5% donkey Serum [Sigma-Aldrich] in 1% BSA/PBS/0.1% Tween) for 1 hour before overnight incubation with primary antibody at 4°C. The slides were washed three times in PBS for 5 minutes and then for immunofluorescence (IF) incubated with appropriate fluorescent secondary antibodies for 45 minutes in blocking buffer. For IF stains for GFP and JUNB, tyramide amplification was used (AF488 Tyramide SuperBoost Kit, Thermo Fisher Scientific) according to kit specifications. Slides were then washed and incubated with 1 $\mu\text{g}/\text{ml}$ DAPI for 10 minutes in PBS and then mounted with Prolong Gold antifade with DAPI (Invitrogen), for IF.

To process immunohistochemistry (IHC) samples, appropriate biotinylated secondary antibodies (Vector Labs) were used with the Vectastain Elite ABC-HRP reagent (Vector Labs) and Diaminobenzidine-reaction kit (Vector Labs) to develop the IHC signal. Harris modified hematoxylin (Fisher Scientific) was used to counterstain nuclei. Finally, slides were washed, dehydrated, and mounted using Vectamount (Vector Labs). TUNEL assay was performed using the *In Situ* Cell Detection Kit, TMR red (Sigma Aldrich) according to manufacturer's instructions.

RNA *In Situ* Hybridization

RNAscope Multiplex Fluorescent Detection kit v2 (ACDbio) in combination with TSA Fluorescein and Cyanine3 Plus Evaluation kits (Perkin Elmer) were used for RNA *in situ* hybridization according to manufacturer's instructions. Before mounting, the slides were counterstained with a primary antibody against pCK or KRT19 for 1h at RT, and then processed as described for the IF methods. Probes for *TdTomato* and murine *Cyr61*, *Klf6* and *Hes1* were used (ACDbio).

Microscopy

IHC images were taken on a Zeiss Axio scope. IF images were obtained on a Zeiss AxioObserver Z1 or on a Zeiss LSM 700 Laser Scanning Confocal microscope. Organoids were visualized by a Nikon SMZ18 and a Zeiss AxioObserver Z1 with Apotome. Composite IF images are indicated by colored text that corresponds to each respective overlaid channel within the image.

Single-Cell Organoid Forming Assay

Single BECs were sorted directly into a 96-well plate (1 cell/well) containing organoid media with 5% Geltrex (Thermo Fisher Scientific, LDEV-Free, hESC-Qualified, reduced growth factor basement membrane matrix) as previously described (Bin Li et al., 2017). Organoid forming percentage was determined 14 days after plating. Organoid media consisted of a 1:1 mixture of L-WRN conditioned media generated as described previously (Miyoshi and Stappenbeck, 2013) and fresh 2X-Media (Advanced Dulbecco's modified Eagle's medium /F12 medium [Invitrogen], 10^3 U/ml; 10^3 $\mu\text{g}/\text{ml}$ Penicillin/Streptomycin [Invitrogen], 2 mM L-Glutamine, 2x N2-supplement [Invitrogen], 2 \times B27 without vitamin A supplement [Invitrogen], 20 mM nicotinamide [Sigma-Aldrich], 0.002 mM dexamethasone [Sigma-Aldrich], 10 mM HEPES [Invitrogen], 20 μM Y27632 [Sigma-Aldrich] (only upon initial derivation and upon passage), 50 ng/ml rmEGF [R&D Systems], 40 ng/ml rmHGF [Peprotech], and 1:500 Primocin [Invitrogen]).

RNA Isolation and quantitative RT-PCR

RNA was isolated using Trizol Reagent (Life Technologies) or NucleoSpin® RNA XS (Macherey-Nagel) according to manufacturers' instructions. Isolated RNA was reverse transcribed for real-time quantitative PCR (qRT-PCR) by an iScript™ cDNA Synthesis Kit (Bio-Rad). qRT-PCR was performed on One Step plus Sequence Detection System (Applied Biosystems) using Fast SYBR® Green Master Mix (Life Technologies). Gene expression data was normalized to *Gapdh*. qRT-PCR primer sequences are listed in Table S7.

Bulk RNA-Sequencing

RNA was isolated from FACs sorted BECs using the NucleoSpin® RNA XS Kit (Macherey-Nagel) according to the manufacturer's instructions. Libraries were prepared on the same day using TruSeq RNA Library Preparation Kit v2, Set B (Illumina). Quantitative PCR and TapeStation to assess library concentration were run by the Biopolymers facility at Harvard Medical School. Samples were sequenced using an Illumina NextSeq 500 with Mid Output kit v2 for 56 cycles.

QUANTIFICATION AND STATISTICAL ANALYSIS

BEC scRNA-Seq Computational Analysis

Reads from BEC scRNA-seq were mapped using bwa mem-0.7.10 with default parameters to the reference transcriptome (*Mus musculus* 10) after extraction of the corresponding cell-specific barcode and unique molecular identifier (UMI). The number of unique transcripts per gene for each cell-specific barcode was extracted from the UMI count as previously described in Grün et al. (Grün et al., 2016). We hence refer to transcripts as unique molecules based on UMI correction. In a first filtering step, only cellular barcodes with more than 1000 mapped reads were kept (1228, 1249 and 1304 barcodes in homeostatic mice 1, 2, and 3 respectively; 1517 barcodes in DDC). Next, cellular barcodes with more than 20% mitochondrial transcripts were discarded. We ran RaceID3 (Herman et al., 2018) to downsample transcript count per cell to 700, and we subsequently removed genes that are present only in 2 cells or

less than 5 transcripts or less. The remaining 286 genes (from originally 14,193 genes found in the raw data) were used to build a t-distributed stochastic neighbor-embedding (t-SNE) map based on Pearson-correlation distances between cells. Non-BEC contaminants, and highly stressed cells (identified as those where heat-shock proteins represent > 1.25% of the whole transcriptome), were identified and removed. The robustness of the data-set was tested with two batch correction algorithms, scran and the one included in RaceID3 (Haghverdi et al., 2018; Herman et al., 2018). Unsupervised clustering (k-medoids) was performed using RaceID to identify subpopulations. To generate the heatmap in Figure 1D, the cells in the x axis were ordered left to right according to their y-coordinate in the t-SNE from Figure 1C (bottom to top). This strategy, to order the cells in that way, was confirmed by performing hierarchical clustering and unsupervised k-medoids clustering (using RaceID3) of the cells based on their gene expression. Both independent clustering approaches identified cellular populations that were ordered along the y axis of the t-SNE. The 286 genes on the y axis were hierarchically clustered by their z-scores (with maximum value set to 3). Genes in clusters annotated with numbers 1, 2 and 5, which show opposing gradients in the average gene expression, were used to define a distinct BEC subset A (26% of cells) and subset B (74%). These gene selections were consistent with the ones defining the cellular subpopulations obtained by k-medoid-based and hierarchical-based clustering. For Figure 1E, a differential gene expression analysis between cell subsets A and B was performed (Table S3) to rank the significant differentially expressed genes based on log₂ fold-change and to compare with the top 600 expressed genes from Yap overexpression in the liver (Dong et al., 2007) by GSEA3.0. In Figure 1F, gene ontology analysis of these differentially-expressed genes was performed using EnrichR (Chen et al., 2013). In Figures S3B and S3C for the construction of the t-SNE map, the DDC dataset was combined with the BEC control data.

The sequencing data of the targeted amplification was mapped in the same way. For Figure S7B, cells were stratified according to their YAP status (subset A versus subset B from Figure 1D), and the distribution of number of detected UMIs per cell was computed for each of the targeted genes. Significance was assessed using Kolmogorov-Smirnov test.

Hepatocyte scRNA-Seq Computational Analysis

Read alignment was performed as in (Macosko et al., 2015). Briefly, for each NextSeq sequencing run, raw sequencing data was converted to demultiplexed FASTQ files using bcl2fastq2 based on Nextera N700 indices corresponding to individual samples/arrays. Reads were then aligned to mm10 genome using the Galaxy portal maintained by the Broad Institute for Drop-Seq alignment using standard settings. Individual reads were tagged according to the 12-bp barcode sequencing and the 8-bp UMI contained in Read 1 of each fragment. Following alignment, reads were binned onto 12-bp cell barcodes and collapsed by their 8-bp UMI. Digital gene expression matrices (e.g., cell by gene tables) for each sample were obtained from quality filtered and mapped reads and UMI-collapsed data and were utilized for further analysis. Barcodes with more than 40% and 80% mitochondrial transcripts in the control and the DDC samples, respectively, were removed.

The number of unique transcripts per gene for each cell-specific barcode was extracted from the UMI count as previously described in Grün et al. (Grün et al., 2016). We hence refer to transcripts as unique molecules based on UMI correction. In a first filtering step, only cellular barcodes with more than 1000 mapped reads were kept (5221 barcodes for adult control mouse and 3192 barcodes for DDC-treated mouse). RaceID3 (Herman et al., 2018) was run to downsample transcript count per cell to 700, and subsequently non-hepatocyte contaminants were removed and genes that were present only in 2 cells or less than 5 transcripts or less. The remaining 277 genes (from originally 16,874 genes found in the raw data) were used to build a t-SNE map based on Pearson-correlation distances between cells.

To generate the heatmaps in Figure 4A and Figure S3G, both homeostatic and DDC cells in the x axis were ordered left to right according to zonation using the algorithm described in (Halpern et al., 2017). In Figures S3F and S3H-I, for the construction of the t-SNE map, the DDC dataset was combined with the adult hepatocyte control data.

Bulk RNA-Sequencing Computational Analysis

Raw sequence reads were processed using Trimmomatic-0.33 with the following parameters: TRAILING:25 MINLEN:35. Sequences were aligned using STAR aligner to the mouse genome: mm10. Gene counts were determined using FeatureCounts. Differential analysis between samples was performed by normalizing read counts using DESeq2 in RStudio and examining significantly expressed genes $\text{padj} < 0.05$. Heatmap was generated using pheatmap (v. 1.0.8) in RStudio. Gene ontology analysis of differentially-expressed genes was performed using the DAVID Bioinformatics database (Huang et al., 2009).

ChIP-Seq Data Analysis

ChIP-Seq data was re-analyzed from previously published data (Galli et al., 2015). Data was aligned to the human genome hg19 using the UCSC genome browser.

Quantification / Statistical Analysis

Power calculations were not routinely performed; however, animal numbers were chosen to reflect the expected magnitude of response considering the variability observed in previous experiments. For quantification of sections, in general, 5-10 random portal fields of each liver sample were imaged and then quantified using Fiji software. Data presented are expressed as mean \pm standard deviation (SD) unless otherwise specified. Data other than sequencing data were analyzed and plotted using Prism Software 8.0 (GraphPad). Technical and biological replicates are specified for each experiment in the figure legends. P values are presented as

follows: * $p < 0.05$, ** $p < 0.01$, *** $p < 0.001$, **** $p < 0.0001$, and were determined by two-tailed Student's t test, unless otherwise specified in the figure legends. When comparing more than two means, significance was assessed by ANOVA, followed by Tukey multiple comparisons test. To compare differences of cellular distribution in regard to mRNA-dots per cell as obtained by RNA-ISH data, the Kullback-Leibler test was performed. FlowJo software was used for all flow-cytometry analysis. Figures were generated using Adobe Illustrator.

DATA AVAILABILITY

The scRNA-seq data (BECs and hepatocytes) and the bulk RNA-seq data (BECs) are deposited in the Gene Expression Omnibus database under accession number GEO: GSE125688.

Supplemental Information

**Single-Cell Analysis of the Liver Epithelium
Reveals Dynamic Heterogeneity and an Essential
Role for YAP in Homeostasis and Regeneration**

Brian J. Pepe-Mooney, Michael T. Dill, Anna Alemany, Jose Ordovas-Montanes, Yuki Matsushita, Anuradha Rao, Anushna Sen, Makoto Miyazaki, Sayeepriyadarshini Anakk, Paul A. Dawson, Noriaki Ono, Alex K. Shalek, Alexander van Oudenaarden, and Fernando D. Camargo

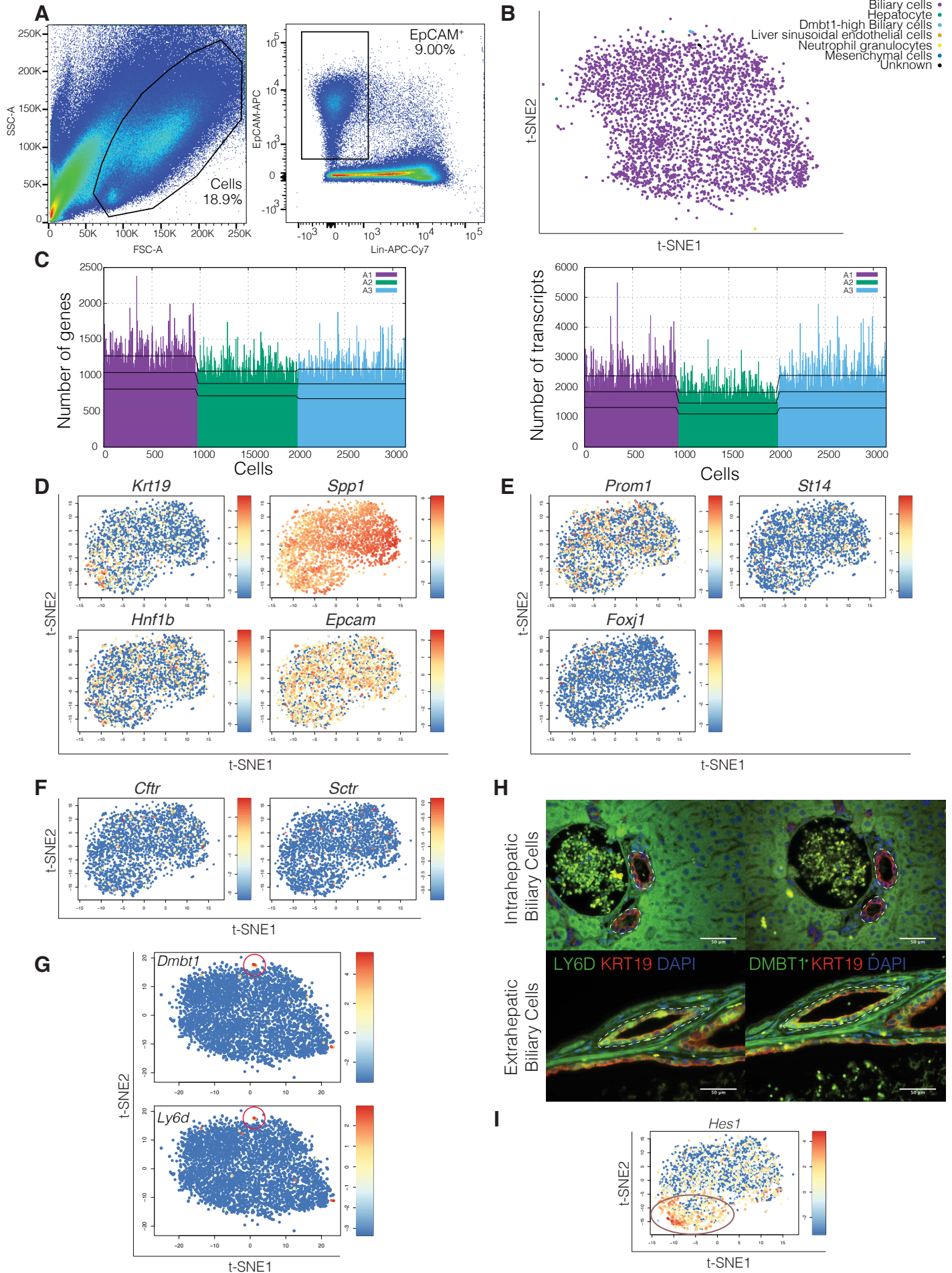
Figure S1

Figure S1. Extended Analysis of ScRNA-Seq Data for BECs, Related to Figure 1.

(A) Gating strategy for isolation of BECs by FACS. BECs were sorted on forward scatter (FSC) and side scatter (SSC) and subsequently by EpCAM⁺, Lin⁻ (CD11b, CD45, TER119) and DAPI⁻. Approximately 1500 cells per sample were encapsulated with the inDrops platform and analyzed by next generation sequencing.

(B) t-SNE plot of all three combined homeostatic BEC samples identifying non-biliary cells by different colors, which were subsequently excluded from further analysis.

(C) Histograms showing number of annotated genes per cell (Left) and number of transcripts per cell (Right) across three adult homeostatic BEC scRNA-seq samples. Different libraries are indicated in different colors. The black horizontal lines indicate the mean \pm SD for each library.

(D) t-SNE plots showing expression in log₂ scale of the common biliary markers *Krt19*, *Spp1*, *Hnf1b*, and *Epcam*.

(E) Expression of the previously proposed biliary progenitor markers *Prom1*, *St14*, and *Foxj1*, as represented by t-SNE.

(F) t-SNE plots of genes previously found to correlate with large, distal BECs, *Cftr* and *Sctr*. Colors denote relative expression of respective gene in each cell.

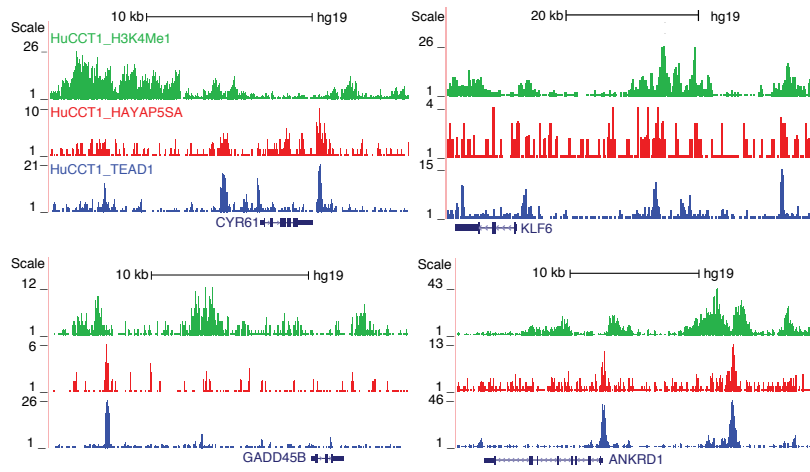
(G) Identification of a populations of extrahepatic biliary cells marked by *Dmbt1* and *Ly6d* expression, as represented by t-SNE. Red circle highlights a small cluster of cells identified by RaceID3 that highly co-express *Dmbt1* and *Ly6d*.

(H) IF for LY6D/KRT19/DAPI and DMBT1/KRT19/DAPI in intrahepatic and extrahepatic BECs. Positive DMBT1 and LY6D signal is only observed in extrahepatic BECs.

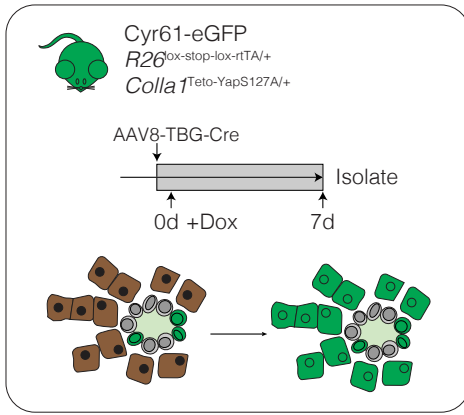
(I) t-SNE plot showing expression in log₂ scale of *Hes1*. Colors denote relative expression of respective gene in each cell.

Figure S2

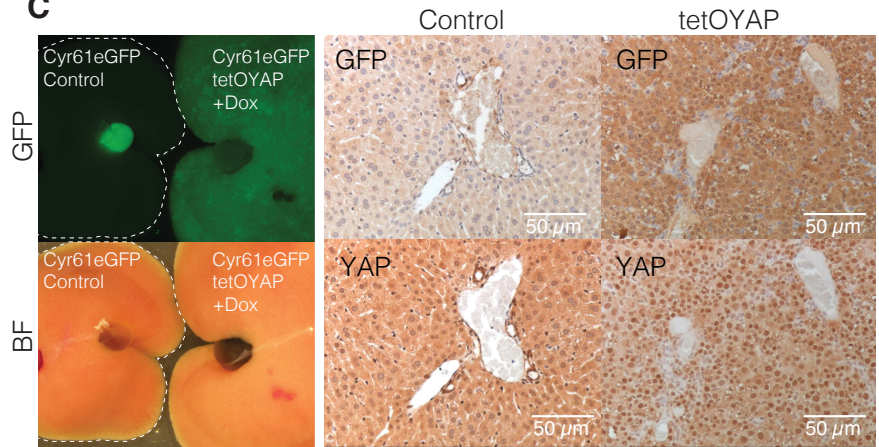
A



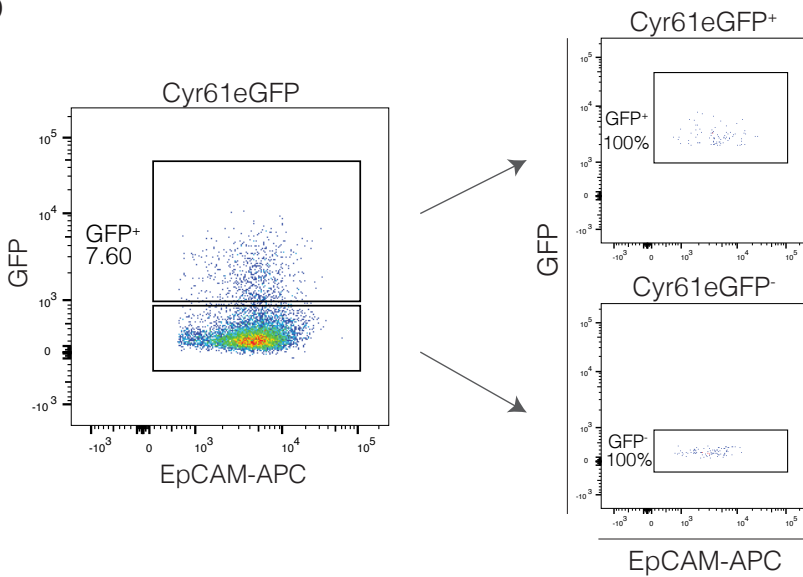
B



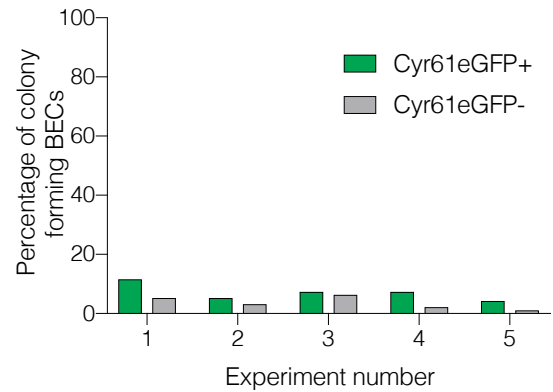
C



D



E



F

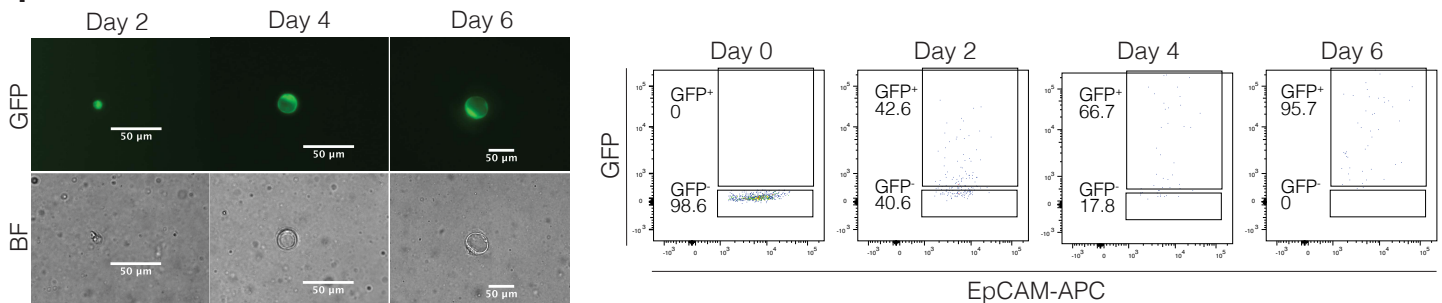


Figure S2. Genomic Tracks of ChIP-seq Data and Supplementary Data for Cyr61eGFP Mouse Experiments, Related to Figure 2.

(A) Genomic tracks displaying ChIP-seq data for YAP^{5SA} (constitutively-active YAP), TEAD1, and H3K4Me1 in a human liver cholangiocarcinoma cell line, HuCCT1, around the genomic location of genes *CYR61*, *GADD45B*, *KLF6*, and *ANKRD1* identified by scRNA-seq as associated with YAP activity.

(B) Schematic showing genetic mouse model used to examine Cyr61eGFP YAP responsiveness *in vivo*. Cyr61eGFP mice were crossed to *TetOYap* mice (*R26^{lox-stop-lox-rtTA/+}; Col1a1^{tetO-YapS127A/+}*), which allows for doxycycline inducible expression of constitutively active, YAP^{S127A}. These mice were administered AAV8.TBG.PI.Cre.rBG (AAV-Cre) at a dose of 1×10^{11} GC and given doxycycline for 1 week to overexpress of YAP^{S127A} specifically in hepatocytes.

(C) Left: Fluorescence and bright field images confirm upregulation of GFP in CYR61eGFP; *TetOYAP* mouse livers as a surrogate for active YAP overexpression upon doxycycline administration compared to control. The bright fluorescent spot in the CYR61eGFP only mouse represents the gallbladder containing fluorescent bile. This is not seen in the *TetOYAP* mouse liver, where bile usually assumes a darker color. Right: IHC of serial sections for GFP, YAP, and pCK in Cyr61eGFP and Cyr61eGFP; *TetOYAP* livers. Active, nuclear YAP is visible in *TetOYap* livers with concurrent GFP upregulation.

(D) FACS plot of EpCAM⁺ BECs from Cyr61eGFP mouse livers which were sorted into GFP⁻ and GFP⁺ populations and plated each in a 96-well plate at a single cell per well. Purity was confirmed in a double sort as indicated in the additional FACS plots.

(E) Bar plot showing percentage of wells that contained colonies 14 days after seeding (n=5 replicative experiments).

(F) Left: Representative fluorescent and bright field images of biliary organoids sorted from EpCAM⁺ GFP⁻ cells from Cyr61eGFP mouse livers at the indicated time points after seeding. Right: Representative FACS plots of originally 5000 GFP⁻ BECs sorted into each organoid well and monitored by FACS for GFP expression at 2 days, 4 days, and 6 days after plating.

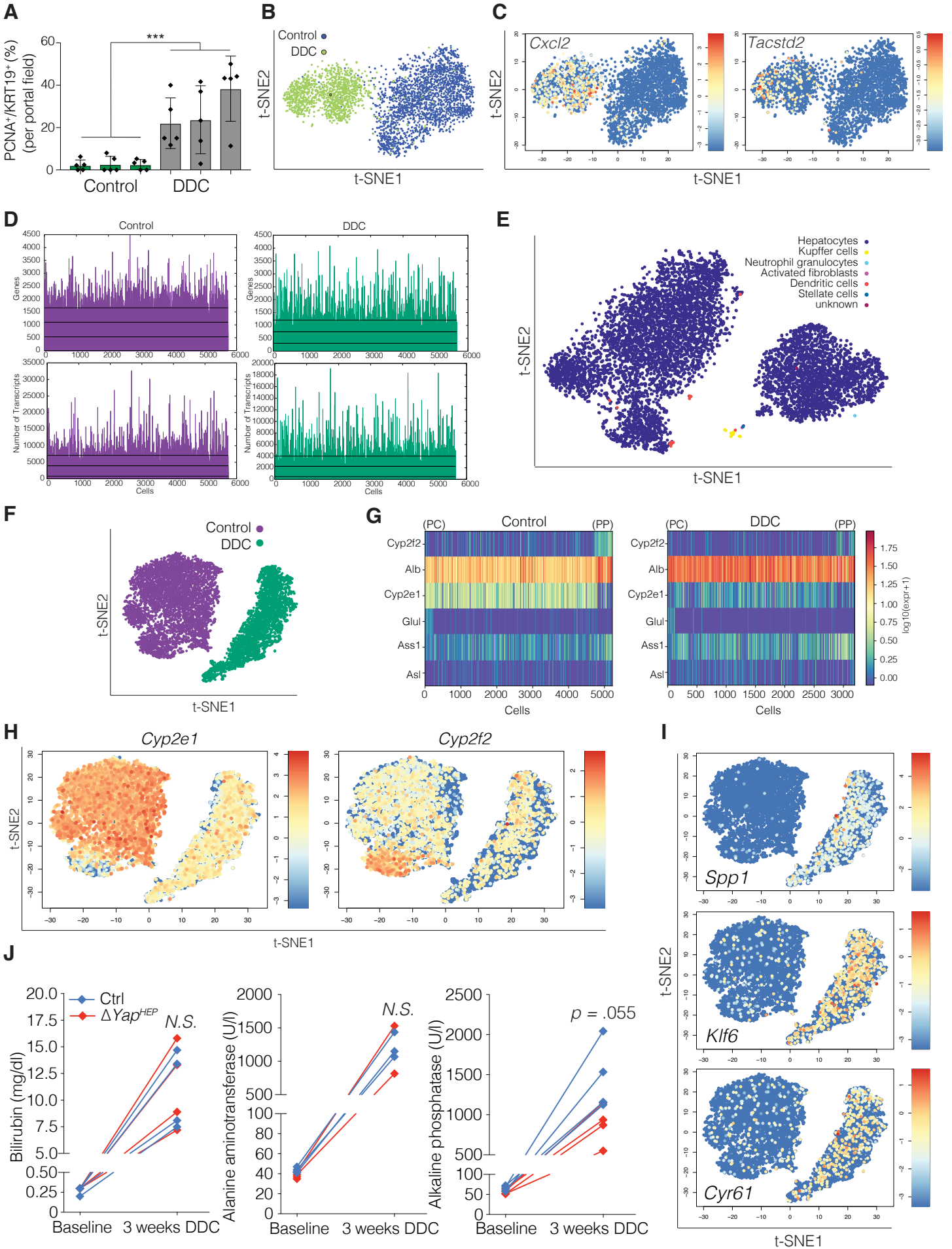
Figure S3

Figure S3. Extended Data From scRNA-seq Analyses of DDC-Injured BECs and Hepatocytes, Related to Figures 3 and 4.

(A) Bar-scatter plot indicating the number of PCNA+ BECs assessed by IF of mice fed with standard or DDC-supplemented feed for 1 week. Data are mean \pm SD of 5 portal fields per mouse (n = 3 mice per group).

(B) t-SNE plot comparing scRNA-seq data from homeostatic (**Figure 1C**) (blue) and DDC-injured BECs (green).

(C) Expression of *Cxcl2* and *Tacstd2*, two well-known upregulated genes upon DDC injury, as represented by t-SNE. Colors denote relative expression of respective gene in each cell (log₂ scale).

(D) Histograms showing number of transcripts per cell and number of annotated genes per cell across homeostatic and DDC-injured hepatocytes from the scRNA-seq samples. The black horizontal lines indicate the mean and mean plus/minus standard deviation for each library.

(E) t-SNE plot of combined hepatocyte samples (control and DDC) identifying non-biliary cells by different colors, which were subsequently excluded from further analysis.

(F) t-SNE plot of scRNA-seq data comparing homeostatic (purple) and DDC-injured hepatocytes (green).

(G) Heatmap of landmark zonation genes evaluated according to the algorithm of Halpern et al. (Halpern et al., 2017) for single hepatocytes isolated from homeostatic and DDC injured livers. Colors denote normalized expression in log₁₀ scale of respective gene in each cell. Cells in the x axis are ordered according to relative distance to the pericentral (PC) vein area (left) and the periportal (PP) area (right).

(H) Normalized expression in log₂ scale of two well-known hepatocyte zonation genes *Cyp2e1* and *Cyp2f2* as represented by t-SNE of the merged hepatocyte samples (control left, DDC right).

(I) Normalized expression (in log₂ scale) of the ductal marker *Spp1* and of two YAP target genes, *Cyr61* and *Klf6* as represented by t-SNE.

(J) Timeline of blood chemistry analysis of ΔYap^{HEP} mice and controls at baseline and 3 weeks after DDC diet for bilirubin, alanine aminotransferase (ALT) and alkaline phosphatase (n = 4 mice per group).

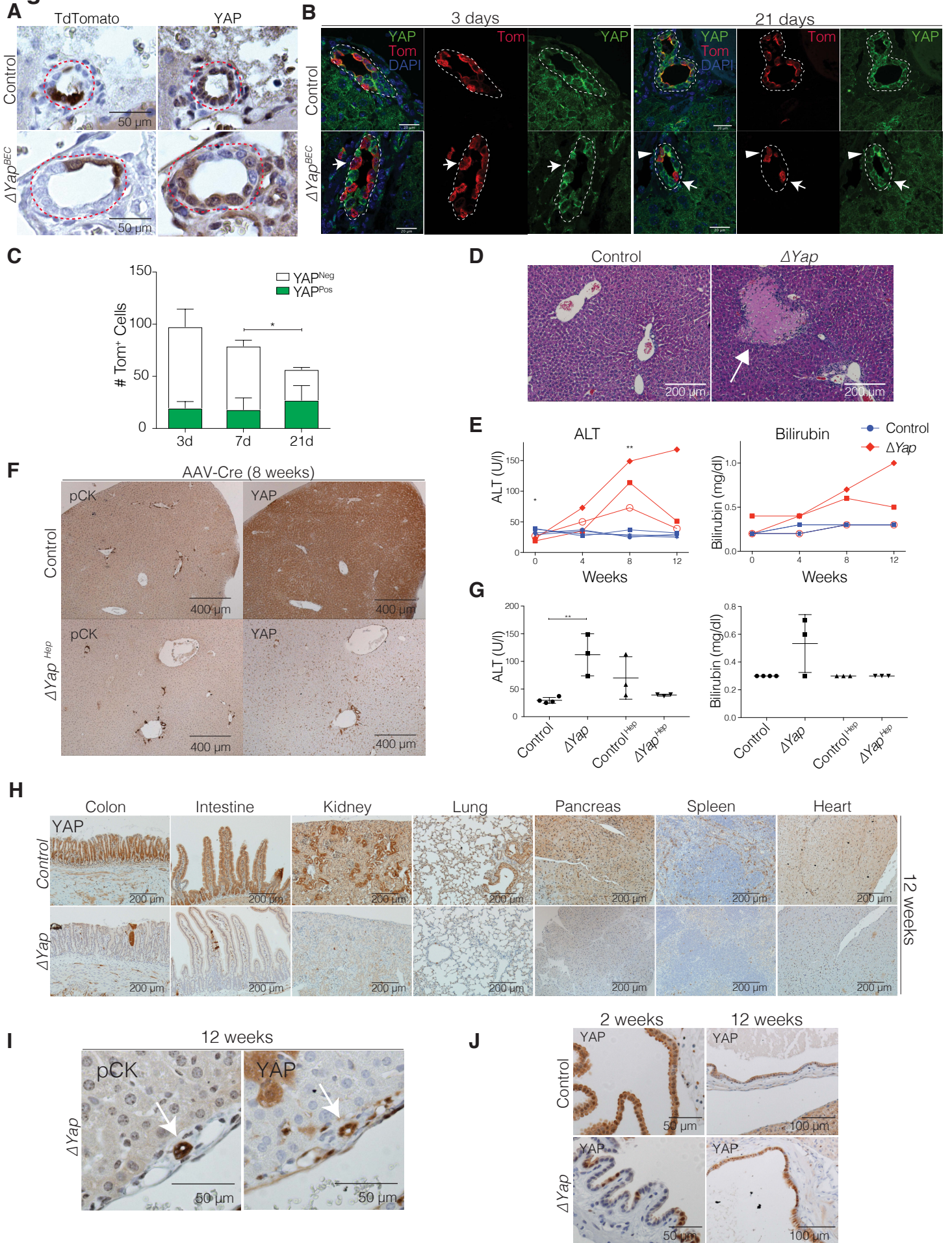
Figure S4

Figure S4. Effects of Inducible *Yap* KO in BECs, Hepatocytes and All Cells, Related to Figure 5.

(A) Immunostaining for Tom and YAP in serial liver sections depicting bile ducts from ΔY_{ap}^{BEC} and Control mice, 3 days after TAM, demonstrating average *Yap* KO efficiency of ~40%. Dashed lines outline bile ducts.

(B) IF of YAP and Tom, at the indicated time points after *Yap* KO. Arrows indicate Tom⁺ YAP⁻ cells. Arrowheads illustrate escaper YAP⁺ Tom⁺ cells at 21 days. Dashed lines highlight bile ducts.

(C) Bar plot illustrating the absolute number of YAP⁺ and YAP⁻ cells within the Tom⁺ cell population. A decrease in the total number of YAP⁻ cells over time is observed. Data are mean \pm SD for 10 portal areas of 2 mice per group.

(D) Low magnification H&E images of ΔY_{ap} livers 12 weeks after start with Dox. Arrows indicate patches of necrosis.

(E) Serial blood chemistry analysis for alanine aminotransferase (ALT) and bilirubin levels of ΔY_{ap} and Control mice at the designated weeks after start of Dox (n = 3 mice per group). Each line represents a mouse.

(F) Immunostains for pCK and YAP 8 weeks after administration of AAV-Cre (1×10^{11} GC) to *Yap*^{fl/fl}; R26^{LSL-TdTomato/+} (ΔY_{ap}^{Hep}) and R26^{LSL-TdTomato/+} (Control^{Hep}) control mice without observable biological differences.

(G) Blood chemistry analysis (bilirubin and ALT) for ΔY_{ap}^{Hep} , ΔY_{ap} , and control mice 8 weeks after recombination. Data are mean \pm SD with each symbol representing a mouse.

(H) Immunostains for YAP of indicated tissues from ΔY_{ap} and Control mice 12 weeks after Dox. No pathological morphology was observed in H&E stains of the selected tissues.

(I) Serial immunostains for pCK and YAP of a portal field from a ΔY_{ap} mouse showing escaper YAP⁺ BECs (arrows) at the 12-week time point after the start of Dox.

(J) Representative immunostains for YAP from gallbladder in ΔY_{ap} and control mice 2 and 12 weeks after start of Dox, indicating significant repopulation by Yap⁺ escaper cells over time.

Figure S5

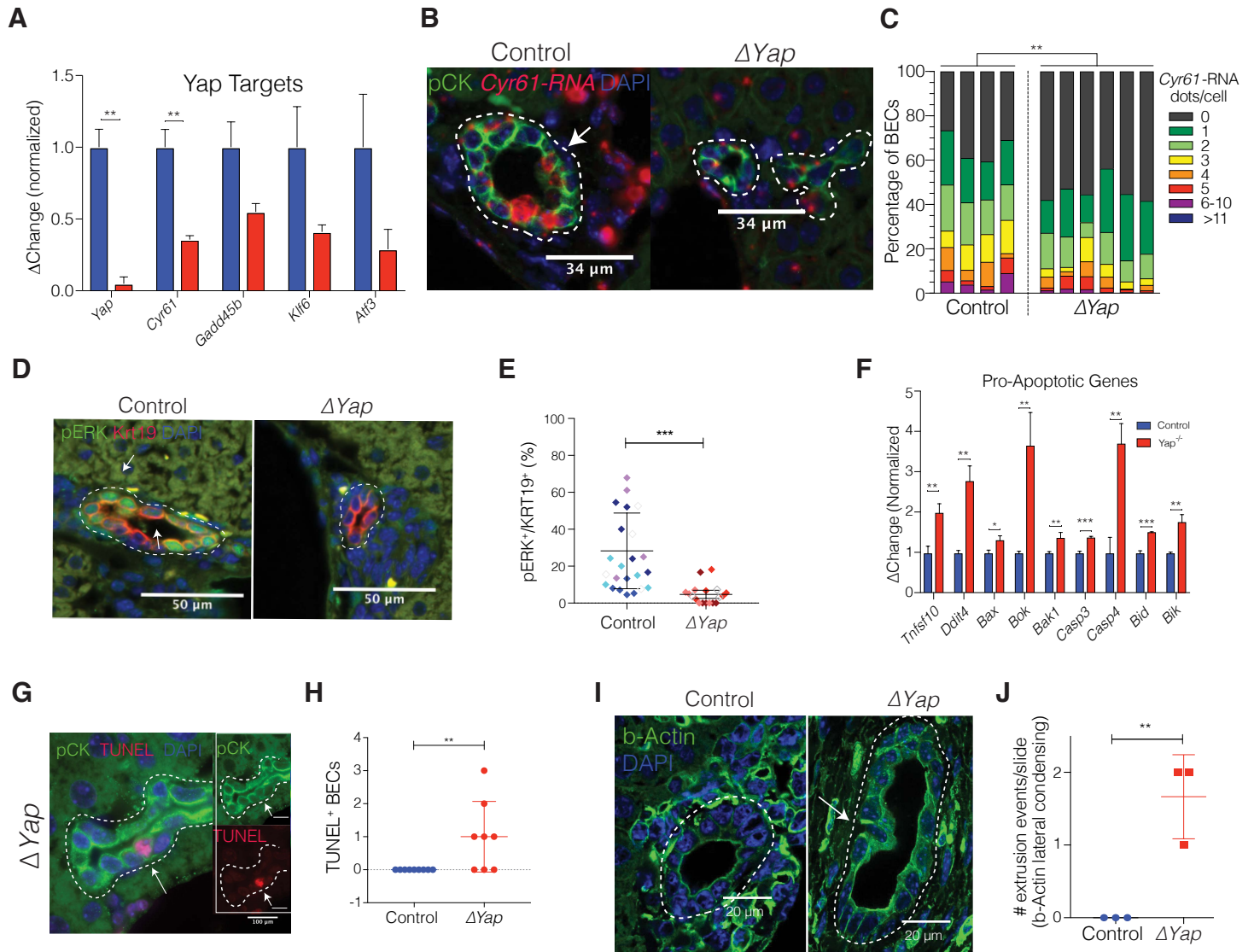


Figure S5. Evaluation of the transcriptional changes upon *Yap* KO in BECs and Cell Death, Related to Figure 5.

(A) qRT-PCR of bulk RNA from sorted BECs from ΔY_{ap} and control mice. Data are mean \pm SD (n = 3 mice per group).

(B) RNA-ISH for *Cyr61* and co-stained for pCK from ΔY_{ap} and Control mice 2 weeks after the start of Dox. Dotted lines highlight bile ducts. Arrow indicates BEC with high counts of *Cyr61* RNA molecules.

(C) Distribution bar plot of *Cyr61*-RNA ISH quantification for ΔY_{ap} and Control mice 2 weeks after the start of Dox. Each bar represents a mouse, and BECs are color-coded according to the contained number of *Cyr61*-RNA and shown as percentage of cumulative 6 portal fields counted. P-values were computed using the Kullback-Leibler test.

(D) IF of pERK and KRT19 of ΔY_{ap} and Control mice 2 weeks after the start of Dox. Dotted lines highlight bile ducts and arrows indicate pERK-positive cells.

(E) Quantification of the ratio of pERK⁺ cells per total number of KRT19⁺ cells. Each diamond represents a portal field counted, different colors denote each mouse (5 portal fields per mouse). Indicated are mean \pm SD for three biological replicates.

(F) Fold change of RNA sequencing data of pro-apoptotic genes from BECs upon *Yap* KO. Data are mean \pm SD (n = 3 per group).

(G) IF for pCK and TUNEL assay depicting a bile duct in a ΔY_{ap} mouse 2 weeks after doxycycline administration. Dotted lines highlight bile ducts and arrow illustrates TUNEL⁺ cell.

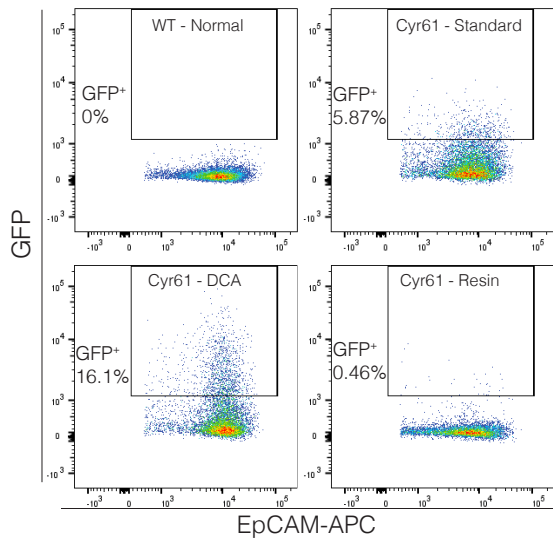
(H) The total number of TUNEL⁺ cells in each portal field per liver section. Data are mean \pm SD with each dot representing a mouse (n = 9 control, n = 8 ΔY_{ap}).

(I) IF for β -Actin on ΔY_{ap} and Control mice show basal actin condensation in a single cell upon *Yap* KO, typical of cellular extrusion. Dotted lines highlight bile ducts and arrow points to extruding cell in ΔY_{ap} sample.

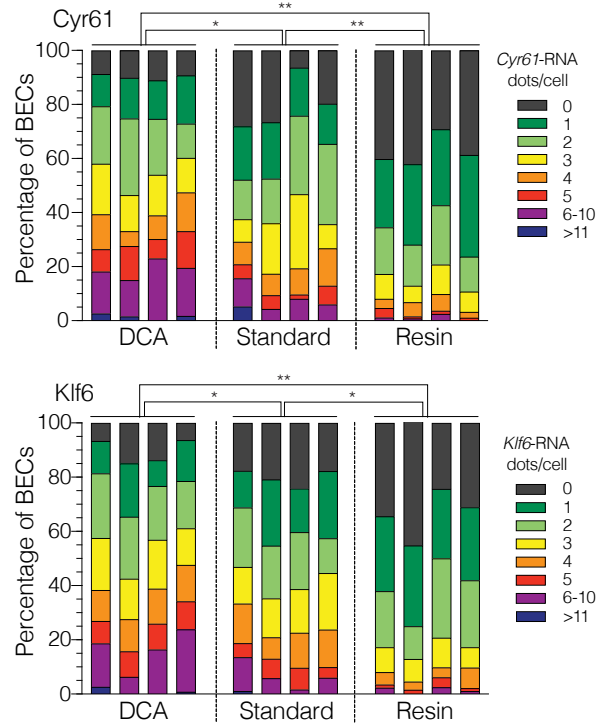
(J) Quantification of the number of extruding BECs per section. Data are mean \pm SD (n = 3 mice per group).

Figure S6

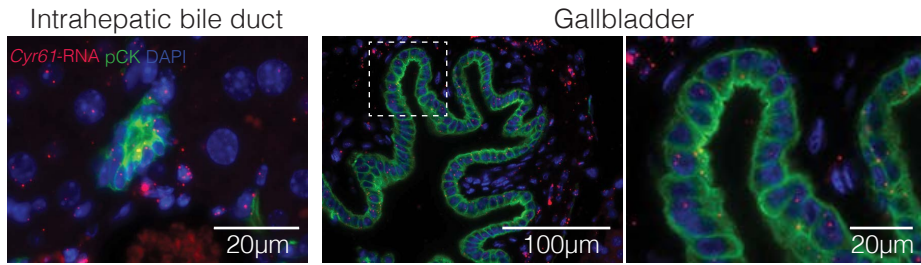
A



B



C



D

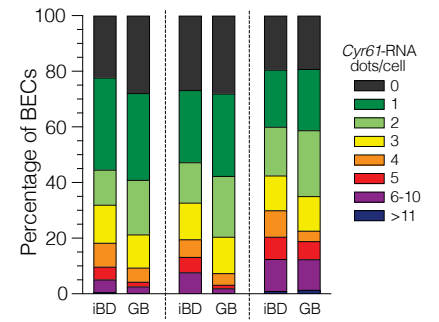


Figure S6. Effect of BA Modulation on YAP-Target Gene Expression, Related to Figure 6.

(A) FACS analysis of isolated EpCAM⁺ BECs from C57Bl/6J (WT) mice administered standard feed and Cyr61eGFP (Cyr61) mice administered standard, DCA, or resin feed, indicating percentage of GFP⁺ cells.

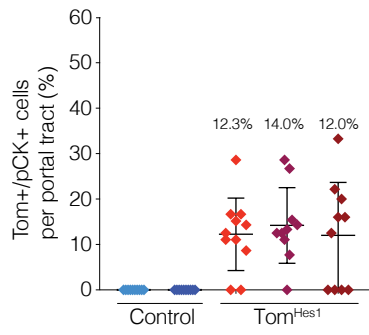
(B) Distribution bar plot of *Cyr61*-RNA and *Klf6*-RNA ISH quantification from **Figure 6E** for the indicated groups. Each bar represents a mouse, and BECs are color-coded according to the contained number of *Cyr61*-RNA and shown as percentage of cumulative 5 portal fields counted. P-values were computed using the Kullback-Leibler test.

(C) Representative images of RNA-ISH for *Cyr61* and co-stained for pCK from intrahepatic bile ducts and gallbladder.

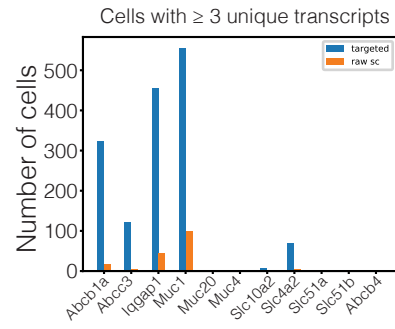
(D) Distribution bar plot of *Cyr61*-RNA ISH quantification of paired intratepatic bile ducts (iBD) and gallbladder (GB) from 3 different mice. BECs are color-coded according to the contained number of *Cyr61*-RNA and shown as percentage of cumulative 5 200X images counted. P-values were computed using the Kullback-Leibler test and were not significant between iBD and GB.

Figure S7

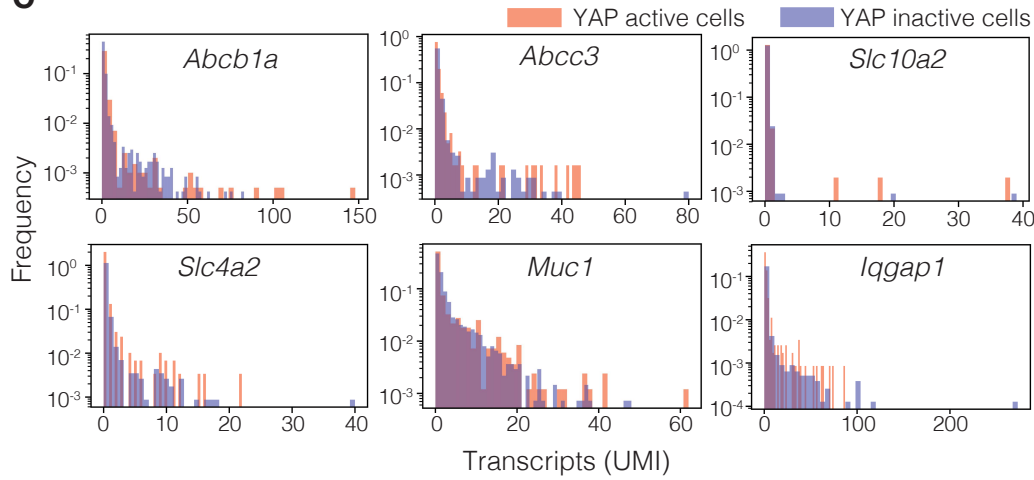
A



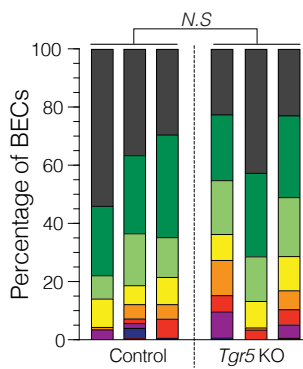
B



C



D



E

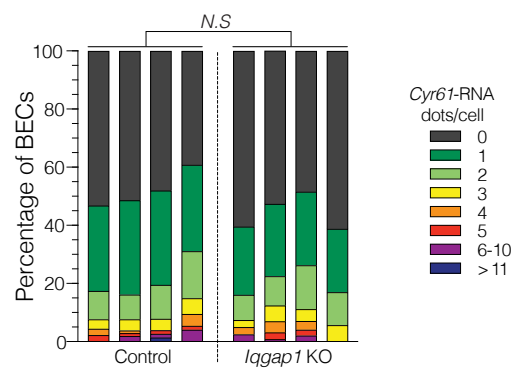


Figure S7. Targeted scRNA-seq Analysis and Evaluation of *Tgr5* and *Iqgap1* KO on YAP targets in BECs, Related to Figure 7.

(A) Scatter plot of the quantification of Tom⁺ BECs per portal tract in Hes1^{CreERT2/+}; R26^{LSL-TdTomato/+} mice (Tom^{Hes1}, n = 3) and R26^{LSL-TdTomato/+} (Control, n = 2), 5 days after administration of 1mg TAM i.p. Each diamond represents a portal tract, indicated are mean ± SD, and average percentage per mouse.

(B) Bar plot depicting the number of cells from the merged control BEC scRNA-seq (Figure 1) containing at least 3 or more unique transcripts for the respective gene in the primary data set (orange) and after targeted amplification (blue). For further information about the selected genes, see **Table S6**.

(C) Histogram of the successfully amplified transcripts from the control BEC scRNA-seq libraries, showing the frequency of cells (y-axis) containing a certain number of unique transcripts (x-axis). Cells are stratified according to their YAP activity as defined in Figure 1, with orange indicating YAP-active cells and blue YAP-inactive cells. No significant differences in expression between the two groups can be observed, and statistical evaluation with Kolmogorov-Smirnov test did not indicate significance for any gene.

(D) Distribution bar plot of *Cyr61*-RNA ISH quantification for *Tgr5* KO and Control. Each bar represents a mouse. BECs are color-coded according to the contained number of *Cyr61*-RNA dots and shown as percentage of cumulative 10 portal fields counted. P-values were computed using the Kullback-Leibler test.

(E) Distribution bar plot of *Cyr61*-RNA ISH quantification for *Iqgap1* KO and Control. Each bar represents a mouse. BECs are color-coded according to the contained number of *Cyr61*-RNA dots and shown as percentage of cumulative 10 portal fields counted. P-values were computed using the Kullback-Leibler test.

Table S2. Genes which define Dmbt1 cluster analysis from scRNA-seq of homeostatic BECs, Related to Figure 1.

Gene Symbol	Mean.ncl	Mean.cl	Fold Change	p-value
Dmbt1	0.1223	24.3249	198.9246	< 2.2E-308
S100a6	0.2392	7.3451	30.7031	2.12E-10
Spink4	0.0908	1.3592	14.9686	0.00388
Ly6d	0.0964	1.3862	14.3785	0.00436
Sfn	0.1273	1.6667	13.0943	0.00744
Plaur	0.1212	1.1800	9.7368	0.00677
Itpkc	0.1314	1.2363	9.4089	0.00791
Tff2	0.2073	1.9164	9.2433	0.01873
Crip1	0.2671	2.2153	8.2952	0.00260
Epha2	0.1747	1.1910	6.8164	0.01359
Wfdc2	0.2827	1.6769	5.9320	0.03314
F3	0.3367	1.8754	5.5697	0.04540
Krt19	0.3157	1.2966	4.1066	0.04047
Cox17	0.3087	1.2236	3.9636	0.03886
Rps23	0.7684	2.4225	3.1527	0.04293
Rn45s	0.7807	2.4416	3.1275	0.04463
Fosb	0.3400	1.0044	2.9546	0.04618
Jund	0.7379	2.0305	2.7517	0.03887
Rps21	1.6381	4.4879	2.7397	0.02577
Ifrd1	0.7638	2.0095	2.6309	0.04230
Rpl41	2.7767	6.4499	2.3229	0.02336
Hspa8	3.1836	0.5187	0.1629	0.04136
Spp1	17.4675	2.0591	0.1179	4.20E-06
Hspa1b	6.7499	0.6337	0.0939	0.00116
Hspa1a	4.1376	0.2009	0.0486	0.01591
Anxa5	3.4001	0.0860	0.0253	0.03330
Alb	4.4723	0.0860	0.0192	0.01138
ApoE	11.0453	0.0860	0.0078	1.55E-05

Table S6. List of Genes Selected for Targeted Amplification from scRNA-seq libraries, Related to Figure 7.

Gene ID	Alias	Function	Amplification
Transporters			
Slc10a2	Asbt	Main apical BA transporter	
Slc4a2	AE2	Main apical bicarbonate exporter	
Abcb4	Mdr2	Basolaterally expressed BA transporter, associated with genetic cholestasis	Unsuccessful
Abcb1a	MDR/TAP	Member of MDR/TAP subfamily, basolateral efflux pump of modified BAs and xenobiotics	
Slc51a	Osta	Basolaterally expressed heteromeric Osta-Ostb exporter	Unsuccessful
Slc51b	Ostb	Basolaterally expressed heteromeric Osta-Ostb exporter	Unsuccessful
Abcc3	Mrp3	Involved in basolateral BA efflux, expression induced in cholestasis	
Receptors			
Iqgap1		BA induce Iqgap1 expression which in turn upregulates Yap in hepatocytes (exact mechanism unknown)	
Gpbar1	Tgr5	G-coupled-receptor specific for BA	Unsuccessful
Mucins			
Muc1		Main Mucin, membrane-anchored	
Muc4		Evidence for focal expression in small bile ducts, membrane-anchored	Unsuccessful
Muc20		Expression pattern unknown, membrane-anchored	Unsuccessful

Table S7. Primer Sequences, Related to STAR Methods.

Murine genotyping primer sequences		
Genotype	Direction	Sequence 5' to 3'
Col-YapS127A	Forward (Common)	CCCTCCATGTGTGACCAAGG
	Reverse (Wildtype)	GCACAGCATTGCGGACATGC
	Reverse (Mutant)	GCAGAAGCGCGGCCGTCTGG
Krt19-CreER	Forward (Wildtype)	TCTCGCCTCCTACTTGGACAA
	Forward (Mutant)	CTATCGCCTTCTTGACGAGTT
	Reverse (Common)	ATATCCCTGACTATCCAAGCA
Rosa26-TdTomato (Jax 007909)	Forward (Wildtype)	AAGGGAGCTGCAGTGGAGTA
	Reverse (Wildtype)	CCGAAAATCTGTGGGAAGTC
	Forward (Mutant)	CTGTTCTGTACGGCATGG
	Reverse (Mutant)	GGCATTAAAGCAGCGTATCC
Rosa26-rtTA	Forward	GGACGAGCTCCACTTAGACG
	Reverse	AGGGCATCGGTAAACATCTG
Cyr61eGFP	Forward	CGACAGAGCTACGTCACTGCAACAC
	Reverse	GGTCGGGGTAGCGGCTGAA
Rosa26	Forward (Wildtype)	GGAGCGGGAGAAATGGATATG
	Forward (Mutant)	AAGACCGCGAAGAGTTTGTC
	Reverse (Common)	AAAGTCGCTCTGAGTTGTTAT
Yapfl/fl	Forward (Common)	AACCACCAAACCTGGCATAG
	Reverse (Wildtype)	GAGGCCAAACCTGACAACATA
	Reverse (Mutant)	GTGCCCAGTCATAGCCGAATA
CAGs-rtTA3	Forward (Common)	AGTCACTTGTACACAACG
	Reverse (Wildtype)	TGATTATCTGAATTCTGGGATG
	Reverse (Mutant)	CTCTTATGGAGATCCCTCGAC
Cre	Forward	GCGGTCTGGCAGTAAAACTATC
	Reverse	GTGAAACAGCATTGCTGTCACTT
Hes1-CreER	Forward	CGTACTGACGGTGGGAGAAT
	Reverse	TGCATGATCTCCGGTATTGA
Rosa26-TdTomato (Jax 007914)	Forward (Wildtype)	AAGGGAGCTGCAGTGGAGTA
	Reverse (Wildtype)	CTTTAAGCCTGCCCAGAAG
	Forward (Mutant)	ACGTCAATAGGGGGCGTACT
Asbt KO	Forward (Wildtype)	CCAGGAAGAGTCAGTGCTCAAAACC
	Forward (Mutant)	GGGATCTCATGCTGGAGTTCTTCG
	Reverse (Common)	TGAAAGATAGAGGGCAGTCAATGATGG
Tgr5 KO	Forward (Common)	GATGCTGGAGCCACTATATCAGGAC
	Reverse (Wildtype)	GACTGCCCTAGAAGGACCCAGAGAC
	Reverse (Mutant)	GGAACAGAGCACTCTGTGACTTCC
Iqgap1 Ko	Forward (Common)	TTGCAGTCTGTGGCATGTG
	Reverse (Wildtype)	CCTGCTGACAGGTCAATGAT
	Reverse (Mutant)	CCTGCTCTTTACTGAAGGCT

Primer sequences used for RT-qPCR analysis		
Gene	Direction	Sequence 5' to 3'
Apoc1	Forward	AGAGATCCTTAGATCCAGGGTG
	Reverse	TGGCTACGACCACAATCAGG
Cyr61	Forward	AGAGGCTTCCTGTCTTTGGC
	Reverse	CCAAGACGTGGTCTGAACGA
Gapdh	Forward	AAGGTCATCCCAGAGCTGAA
	Reverse	CTGCTTACCACCTTCTTGA
Klf6	Forward	GGGAACAGTTTCTGCTCGGA
	Reverse	CAGGCAGGTCTGTTGCCAAT
Yap1	Forward	CCCTCGTTTTGCCATGAACC
	Reverse	TCCGTATTGCCTGCCGAAAT
Gadd45b	Forward	CTGATGAATGTGGACCCCGA
	Reverse	CCTCTGCATGCCTGATACCC
Atf3	Forward	CTTCCCCAGTGGAGCCAATC
	Reverse	TCATTTTGTCTCCAGTCTTCGC
Primer sequences used for targeted scRNAseq library amplification		
General inDrop forward primer sequence (R1):		
5' TCGTCGGCAGCGTCAGATGTGTATAAGAGACAG "gene-specific-sequence" 3'		
General inDrop reverse primer sequence (R2):		
3' CAAGCAGAAGACGGCATAACGAGATGGGTGTCGGGTGCAG 5'		
Gene	3' Gene-specific sequences for R1 primer	
Slc10a2	5' ACAGCCTGGGTTTCTTCCTG 3'	
Slc4a2	5' CTGCTTTGGGCAGTCATGTC 3'	
Abcb4	5' GCCGCACCTGCATTGTGATC 3'	
Abcb1a	5' ATATGGTGTTTAATCCAAGTC 3'	
Slc51a	5' CTGCCAGACCTGGACTCAGC 3'	
Slc51b	5' ATCCTGGCAAACAGAAATCG 3'	
Abcc3	5' TTCCTTGTGTCAGATGGACTCG 3'	
Iqgap1	5' TGCTTTGGCAGCACCGAGTC 3'	
Gpbar1	5' GGCCACATTGCTCCTGTGTCAG 3'	
Muc1	5' CAGCTTTGGCGGTCTGCTC 3'	
Muc4	5' GGACCCATCCCTCAGTCTGC 3'	
Muc20	5' CCTCTGTGCCAGAAGAACGG 3'	